2024-12-17

Wellbore Positioning in Directional Drilling by Geopotential Field Anomalies

Silva, Luis A

UNIVERSITY OF CALGARY

Wellbore Positioning in Directional Drilling by Geopotential Field Anomalies

by

Luis A Silva

A THESIS

SUBMITTED TO THE FACULTY OF GRADUATE STUDIES

IN PARTIAL FULFILMENT OF THE REQUIREMENTS FOR THE

DEGREE OF MASTER OF SCIENCE

GRADUATE PROGRAM IN GEOMATICS ENGINEERING

CALGARY, ALBERTA

DECEMBER, 2024

Abstract

When navigating the wellbore trajectory, the geomagnetic north can be used to obtain orientation, but interference with other nearby magnetic sources can drastically affect the value of the magnetic azimuth. A potential solution can be found by modelling the local magnetic field.

Modelling the magnetic field can help estimating the magnetic gradient at nearby locations. Changes in orientation for a given location, could be detected by calculating the angle between the estimated and the measured gradient. In principle this should work provided the measurements are taken within the accuracy limits of the modelled field and the amount of time passed after the gradient estimation is short.

To evaluate the possibility of using the anomalous geomagnetic field for orientation, this research required to estimate various sensor errors and the implementation of various algorithms that are required for inertial navigation. Experiments were performed with the sensor in various static positions, and the sensor moving on a track. Magnetometer measurements were used to model the magnetic field, with the intention to provide uncorrelated heading and velocity information. For the case of the moving sensor this information was fused with IMU measurements into an extended Kalman filter

The results for the sensor orientation in various static positions showed that raw field measurements had a heading error of 17°, by modelling the field, the heading error reduced to 10°. For this case the magnetic field was modelled from the measurements from two points separated 1.2 m. A second test was performed by using 2 points separated by 0.60 m. The modelled field for this test produced a maximum orientation error of 7°.

The results for the sensor moving on a track, showed that the heading error was under 8° for the first 6 seconds of input, but the error increased rapidly after that. One of the reasons for this is that the traveled distance obtained from the mechanization deteriorated very rapidly, and this affected the magnetic field modelling. An odometer / drilling rate might help mitigating this problem and the expected heading error is estimated to be under 8°.

Acknowledgements

I want to express my sincere gratitude to my supervisor Dr. JW Kim for his guidance and financial support during my graduate studies. His research interests created inside of me the desire to learn more and to solve the many problems encountered in the directional drilling industry.

I also want to thank Dr. Michael Sideris, who accepted me into the program and was patient with me and from whom I learn so many interesting things. Also want to thank the other professors in the department of Geomatics engineering, thanks for doing what you do, you are very professional and are moving the department ahead.

I would like to express my gratitude to Ali Fatemi who encouraged me to go back to school after being away for many years.

Finally, I also want to express my gratitude to Betzabe for her love, moral support and for preparing so many meals and her patience with me when I was absent from many family gatherings.

Table of Contents

List of Tables

List of Figures

List of Abbreviations

Abbreviations	**Definition**
2D	Two Dimensional
3D	Three Dimensional
AV	Allan Variance
DR	Dead Reckoning
ECEF	Earth-Centered Earth-Fixed Frame
EKF	Extended Kalman Filter
ENU	East, North and Up
GNSS	Global Navigation Satellite System
GPS	Global Positioning System
IMU	Inertial Measurement Unit
INS	Inertial Navigation System
LLF	Local-Level Frame
L-M	Levenberg-Marquardt algorithm
LSQ	Least Squares
MWD	Measuring While Drilling
MEMS	Micro-Electromechanical System
PSD	Power Spectral Density
PVC	Polyvinyl chloride (A type of plastic)
RMS	Root Mean Square
ZUPT	Zero Velocity Update

Chapter 1: INTRODUCTION

In the past, to get to an underground oil/gas reservoir or mineral deposit, the drilling was only performed vertically. Then when horizontal drilling was introduced, it increased the possibility of covering a larger area and reaching to other reservoirs form one well. This reduced the environmental impact as less wells needed to be drilled on the surface, increasing the production, and reducing the operating cost at the same time.(Joshi & Ding, 1991).

Starting from a vertical well, a trajectory or path for the horizontal drill needs to be designed first. Once the trajectory has been defined and considering that this might be a couple of kilometers deep, the drill head must first be positioned at the correct vertical departure point and then steered so it can start drilling horizontally to follow the designed horizontal trajectory. This means that it is very important to know the location and orientation of the drill head. This is achieved by taking measurements while drilling (MWD) (Jamieson et al., 2012).

The navigation inside the wellbore has been done for many years, and there are two methods that have been mainly used. The first one is by geopotential field measurements and the second one is gyroscope-based surveying. Geopotential field method uses a magnetometer and an accelerometer to estimate the position and orientation of the bottom hole assembly (BHA). This method uses the magnetic north to get the azimuth (Ripka, 2001). It is well known that some rocks possess permanent magnetism thus creating magnetic anomalies. These anomalies deform the main geomagnetic field, and if present nearby the borehole, it generates errors in the azimuth estimation and then in the final position (Thorogood & Knott, 1990). Also, the magnetometer might be influenced by the rotation of the drill string and the flow of the drilling fluid (Shelkholeslami et al., 1991; Torkildsen et al., 2004).

Gyroscope-based surveying uses the gyroscope to obtain orientation. The advantage of the gyroscope is that it is not affected by magnetic fields, and it is known to be very accurate for surveying the well bore. The setback of the gyros is that they are affected by the high temperatures and the vibration during drilling and for this reason the drilling must stop, and the gyros are taken out and then inserted back in. The gyros also require having frequent corrections. Gyroscope surveys are only recommended for short-term navigation or where there is a very strong magnetic interference (Estes & Epplin, 2000; A. M. Noureldin, 2002).

When measuring while drilling, i.e., MWD, vibration and high temperatures present a great challenge to the sensors, therefore the drilling must stop to be able to take reliable measurements. When the drilling stops, the location is called a station. The measurements taken from the sensors at the stations, are used to calculate azimuth and inclination. The depth is obtained from the sum of introduced drill pipe lengths.

Micro-Electromechanical System (MEMS) IMU (inertial measurement unit) sensors provide a solution to obtain continuous measurements (not only at the stations), but a good solution must overcome all these challenges.

1.1 Background

A magnetic source always has 2 poles, and these are the North and South poles. In the presence of one or more magnetic sources, there can be 2, 4, 6, 8 or more poles.

The main magnetic field components at any location comes from the Earth's magnetic field, and they vary with the geographic location. The main field is disturbed by the presence of magnetic minerals in the Earth's crust. There are secular and diurnal variations of the Earth's magnetic field. The secular variations are only noticeable for periods of one or more years. This can be seen by a change in the location of the magnetic north pole. Diurnal variations are small and follow a roughly sine wave with maximum amplitude at higher latitudes. This variation is caused by the rotation of the Earth and Solar wind.(Jamieson et al., 2012) The main field is also disturbed in urban areas by electric networks, buildings, and electric devices.

For drilling navigational purposes, the magnetic north could provide the heading, but all these disturbances and variations make the use of the magnetic field very challenging, and this is the purpose of this thesis, to take advantage of these disturbances and use them for navigation be it outdoors, indoors, or underground.

The local magnetic field can be measured with a magnetometer. With these measurements the magnetic field with its anomalies can be modelled. The model can be used to estimate the field at any nearby point. If we have a good knowledge of the surrounding magnetic field, then a magnetometer can be used for navigation by providing attitude and it can also be used to estimate velocity by assuming that a change in the magnetic field is produced by a change in position (the magnetic field is assumed to be static during short time lapses).

1.2 Literature Review

The literature review focused on the research of using the magnetic field for indoor navigation, on how the authors attempted to overcome the difficulties found when using the magnetic field. Some of the authors worked on “learning” the magnetic field.

1.2.1 Indoor Navigation Research:

In recent years, to help with indoor navigation, magnetometer data has been used to supplement the inertial measurements (Chung et al., 2011; Vissiere et al., 2007).

For the case of indoor navigation, magnetometer data has been used to obtain heading information, but in the presence of magnetic anomalies the heading is very inaccurate, specially inside a building where the magnetic field is highly disturbed by the building structure, electrical equipment, and electronic devices present in the site.(Chung et al., 2011) It was found that these magnetic anomalies can be considered constant and therefore they can be used to improve the position estimation.(Vissiere et al., 2007) Instead of obtaining the heading from the magnetic field, magnetic field anomalies can be used to detect if the sensor is moving. This is because the magnetic field is a potential field, and assuming it doesn’t change with time, then it must change with the position. Therefore, a change in the magnetic field can be related to the velocity of the sensor. In other words, if a magnetometer moves then the magnetic measurements must also change, but if it doesn’t move then the measurements won’t change, and this can be used to correct for accelerometer drifts. This technique is applied in the study done by (Vissiere et al., 2007), where the magnetic field is measured and its spatial derivatives are modelled, then this was incorporated along with inertial measurements into an extended Kalman filter. It is important to note that the accelerometer was not used to measure acceleration, but instead, the accelerometer was used along with the gyroscope to estimate the attitude. They obtained good results where anomalies were present, and no improvement whatsoever in the absence of magnetic anomalies. Later the same authors (Vissière et al., 2007), used 4 magnetometers to directly measure the derivatives of the magnetic field and they concluded that, when using only one magnetometer the velocities can be controlled, improving the positional accuracy to 5cm or under. Then by using 4 magnetometers the positional accuracy improved to 2cm or under. Similar results were obtained by (Dorveaux et al., 2011) where only 3 magnetometers were used, the positions and velocities estimated from the magnetometers alone were compared to those measured with a separate laser telemeter and the comparison showed very good results.

The method proposed by (Kok et al., 2013) use a magnetic field that is generated with a magnetic coil, and it is modelled with known parameters. The local earth's magnetic field must be removed from the magnetometer measurements, and these corrected magnetic measurements are used along with the inertial measurements in a particle filter to estimate the position. The positional results are well under 2 cm, only when the distance of the sensor to the coil is less than 40 cm. This is because the magnetic field falls off cubically with the distance.

The previous methods use the physical properties of the magnetic field to estimate the position. Other authors, like (Chung et al., 2011) create magnetic maps inside a building beforehand, and use magnetic anomalies as signatures that can later be used to estimate the position of a robot.

In the study done by (Wahlström et al., 2013), A magnetometer is used to measure the magnetic field at certain positions around an upside-down table with metallic legs. The magnetic field is modelled by "learning" the field from the measurements, and it is later used to find the magnetic sources that are creating the anomalies.

1.2.2 Modelling The Magnetic field:

A stellarator is a machine with electromagnets arranged in the shape of a donut and they produce a strong magnetic field to keep plasma inside and to control plasma particles with the idea to create the necessary conditions for fusion reactions (https://www.energy.gov/science/doe-explainsstellarators). To calculate the magnetic field inside the complicated array of magnetic coils inside the stellarator, Paul Probert creates a set of fourth order polynomials which he calls Maxwell elements (Probert, 2011). These Maxwell elements solve the static current-free Maxwell equations and can be used for the interpolation of the magnetic field. The Maxwell elements solve Laplace and wave equations. In his paper, he creates a 3-D grid and pre calculates the magnetic field on the grid points, then by storing the Maxwell Elements at each grid point, the magnetic field and its gradient can be approximated at any arbitrary point inside the grid. This approximation is accurate and fast. The grid's magnetic field is calculated by using a special Biot-Savart representation of the coils. The grid doesn't need to be regular, but it is necessary to know the magnetic field and its gradients at each grid point. The work of Rodrigo Ramon uses Harmonic Polynomials to expand the scalar potential from where its gradient is calculated (Rodrigo Ramon, 2018). These polynomials satisfy Maxwell's and Laplace's equations. Compared to the Maxwell's Elements, this method only requires measurements of the magnetic field to obtain the scalar potential.

1.2.3 Magnetic & Gravity Surveys for Directional Drilling:

Generally, magnetic and gravity surveys are performed on the earth's surface where directional drilling operations are going to be performed, and this is called In-Field Referencing (IFR). IFR is used to make corrections to magnetometers by using Multi Station Analysis (MSA) and Variable-Reference MSA methods (VR-MSA). The VR-MSA method estimates magnetic reference values at each station using forward and inverse modelling of the IFR data (Kabirzadeh et al., 2018).

1.3 Sensors-based Navigation Strategies

MEMS sensors provide an easy to implement navigation solution. The use of various sensors simultaneously, is referred as to multi-sensor fusion.

The basic combination is to have an accelerometer along with a gyroscope running simultaneously. This is called a Strapdown Inertial Navigation System (SINS). This system starts with an initial position and attitude, then the mechanization equations transform the accelerometers and gyroscopes measurements from body frame to navigation frame and then integrate the acceleration to estimate velocity, then integrates the velocity to find the distance advanced to then find the position. The angular rate is also integrated to find the angular change, to then find attitude. This navigation mode is called dead reckoning (DR).

Without applying corrections to the biases, scale factors and noise to the inertial sensors' measurements the SINS only provides a reliable navigation estimation for a short time as these errors are magnified by the integrations. The reality is that these errors cannot be completely removed, so external aids must be used to make this system usable.

Because accelerometers and gyroscopes are affected by vibration, shock, and temperature during drilling operations, it is a good start to evaluate the accuracy obtained by fusing these sensors in different ways in a lab-controlled environment. As every sensor has its own advantage and disadvantage the goal is to try different configurations to find the best possible. In this thesis two combinations will be tried:

1. Fusion of three-axis accelerometers with the three-axis gyroscopes
2. Fusion of three-axis accelerometers with the three-axis magnetometers

For the second combination, the magnetometer will provide "external" measurements of attitude and velocity. A Kalman filter will estimate the errors of position, orientation, and velocity along with the sensor errors to make corrections to the state vector.

If the magnetometer provides a good source of heading information, the next step will be to work in a solution that mitigates the vibration effects on the sensors. It will be also required to study the behavior of the sensors working under high temperatures, but this is not part of this thesis.

1.4 Thesis Contributions

My most significant contribution to this research, is to allow the use of the local magnetic field for orientation which traditionally has been very difficult to use and not very reliable. Orientation is very important for navigation. Navigation might be required above ground or in a very challenged location, like for example urban canyons, indoors or even in underground environments. This can be achieved by using the magnetic field, with or without the presence of magnetic anomalies. This is not by looking for the geomagnetic north, but by detecting changes in a sensor's orientation. Changes in a sensor orientation can be quantified by modelling the local magnetic field.

1.5 Thesis Objectives

The main objective of this research is to evaluate the usability of a model of the local magnetic field in a lab-controlled environment to improve the positioning and attitude accuracy. The objectives include:

a. Evaluate the use of various sensors working simultaneously.
b. Estimate the deterministic errors and apply the necessary corrections to each sensor.

c. Create a model of the local magnetic field with magnetometer measurements. The model will provide velocity and attitude corrections to the navigation system.
d. Develop a Kalman filter to provide an optimal estimation to the navigation solution.
e. Experimental tests will be performed in a controlled lab environment to facilitate the analysis of the test results and to recommend a navigation solution that could improve the overall accuracy for the wellbore surveying.

1.6 Thesis Outline

The thesis consists of six chapters, Chapter Two will cover the sensors used and the description of their error sources.

The fusion of gyroscopes, accelerometers and magnetometers, the algorithms, and the design of a centralized Kalman filter are described in Chapter Three.

Chapter Four will show the calibration results for each sensor, and it will also discuss the Allan variance analysis performed on the accelerometers and gyroscopes.

1.7 Chapter Summary

Navigation inside the wellbore is very challenging, different methods and sensors are used to overcome these challenges. One of these challenges are the magnetic field anomalies. Some of the authors mentioned in the literature review above, have been applying different methodologies with relatively good success. Thee need for a fast algorithm to accurately guide and electron inside a stellarator encouraged researchers to look for mathematical solutions to properly model the magnetic field. These solutions are the Maxwell elements and the Harmonic Polynomials. The approach for this thesis is to model the measured magnetic field by keeping its physical properties with the use of harmonic polynomials.

Chapter 2: INERTIAL NAVIGATION WITH MEMS SENSORS

The main sensors used for navigation are accelerometers and gyroscopes. This is because the trajectory of a moving object is defined by its position, direction, and velocity. The object's velocity is obtained by the integration of the accelerometer measurements, and the object's rotation is obtained by the integration of gyroscope measurements. To properly describe an object's movement in 3D-Space, its linear acceleration and rotation are both required (El-Sheimy, 2018).

Accelerometers and gyroscopes working simultaneously constitute what is called an inertial measurement unit (IMU). These sensors are micro-electromechanical systems (MEMS). Today's IMU typical sensors contain 3-axis accelerometers, 3-axis gyroscopes, plus 3-axis magnetometers, a thermometer, and a digital barometer. Different sensors placed in a single board, present a great advantage for navigation. An inertial navigation system (INS) takes the raw measurements from the IMU and process them to obtain the changes in an object movement.

An accelerometer measures the linear acceleration and the gravity acting on it. The working principle is based on a proof mass connected to a spring and both are attached to a fixed support or frame. If the frame is moved the proof mass resist to move and the spring is either stretched or compressed. The force on the spring is measured and it corresponds to the acceleration acting on the fixed support. To obtain the linear acceleration, the gravity vector must be removed (El-Sheimy, 2018).

A gyroscope measures the rate of change of angular velocity with respect to a reference frame. MEMS gyros are in their majority of the vibration type, and they consist of a mass-spring system. The working principle consists of a mass vibrated in a plane at an angular rate $\mathbf{\Omega}$, if there is a Coriolis force, then the mass will also vibrate perpendicular to that plane and this vibration is proportional to $\mathbf{\Omega}$ (Barbour, 2010). The Coriolis force is an apparent force that it is observed in a rotating frame of reference. Because these gyroscopes are based on the Coriolis force, they are called Coriolis vibratory gyroscope (CVG). To obtain the angular change, only one integration of the gyroscope output is required. A three-axis gyroscope will measure the Earth's rotation and this needs to be removed to obtain the net angular change.

The dead reckoning method mainly uses the gyroscopes and accelerometer measurements to estimate the position, unfortunately because of the integration of the sensor's bias and scale factors and noise, the positioning accuracy deteriorates very quickly with time. The corrections usually come from a separate source, like GNSS or by an odometer measuring the travelled distance or by computer vision techniques. Another way of making corrections, is when the object is not moving, and this is called a zero update (ZUPT).(A. Noureldin et al., 2012) To reduce these errors, a calibration of the inertial sensors is required. But even with calibration, the inertial measurements must be corrected periodically.

2.1 Inertial Sensor Errors

MEMS sensors are prone to errors. These errors can be classified as deterministic and stochastic.

The fabrication of a sensor is not entirely perfect, and errors are inherent during the manufacturing and mounting process. These errors are deterministic in nature and can be removed by calibration. MEMS sensors' measurements also contain a wide variety of errors that vary randomly with time, among them the bias, scale factor and noise have been identified to be present in the output (Aggarwal, 2010). Figure 1 shows how a physical signal is measured and how it is affected by the sensor errors.

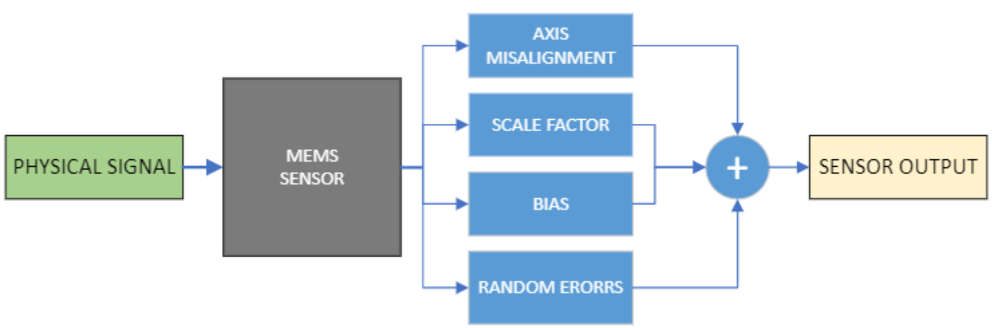

Figure 1. Main errors affecting a physical signal measured by a sensor.

2.1.1 Deterministic Errors

The deterministic errors affecting accelerometer and gyroscopes are described in this section. These are the bias, scale factor and non-orthogonality errors that affect the measurements taken by a MEMS sensor, they greatly reduce the sensor's accuracy. Deterministic errors can be removed through calibration (El-Diasty & Pagiatakis, 2010).

The bias offset can be measured when the input to the sensor is zero and the expected output must also be zero. A different output value means that the measurement is offset by that amount. This amount is constant, and once known it must be removed from all the measurements. The other component of the bias is white noise. Figure 2 shows how far the measurement is from the true value due to the bias offset. The measurement itself shows white noise along the time axis.

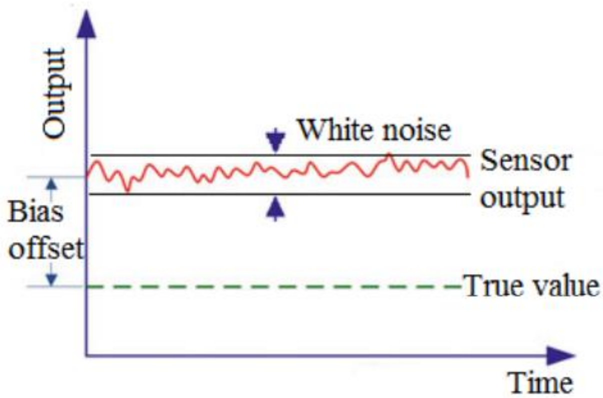

Figure 2. Bias offset separates a measurement from the true value. The measurement itself has white noise (El-Sheimy, Lecture notes 2016)

The scale factor error affects the input signal by scaling it by a factor that ends changing the output. For the accelerometer and gyroscopes this error is proportional to the true input force or angular velocity respectively. When this error is constant in time, it can be removed with calibration.

Non-Orthogonality errors refer to the angles formed between the three sensitive axes for each sensor. These axes must be perpendicular, but there are errors when mounting the sensors at the factory, but also misalignment can happen later in time.

2.1.2 Stochastic Errors

A MEMS sensor output contains a wide variety of random errors. They can only be removed by modelling these errors as a stochastic process. This is because these errors change randomly with time. Two of these errors are the bias and scale factor drift, the other errors can be grouped into stochastic noise. Usually, the word drift is used when changes occur in one run.

The bias drift error is produced by a random change in the bias. This error is difficult to model, and it adversely impacts the accuracy of the measurements (Wall & Bevly, 2005, 2006). Figure 3 shows this error.

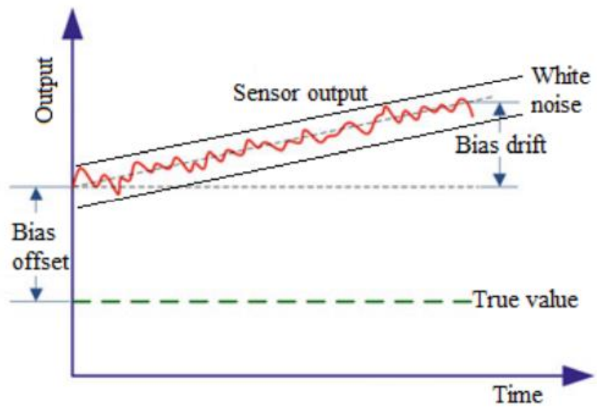

Figure 3. The bias drift error is random and reduces the measurement accuracy (El-Sheimy, Lecture notes 2016)

The scale factor drift error also changes randomly with time from run to run.

The random nature of the errors presented above are very challenging to remove, and they can only be mitigated. The mitigation can be obtained by stochastic process modelling. In stochastic modelling the random process that best suits the error, must be identified first. These random processes are white noise, random constant, random walk, first order Gauss-Markov and auto regressive processes among others. They are detailed in (Gelb, 1974). These random processes are described in Appendix B.

2.2 Allan Variance

The Allan variance (AV) is a method that helps identifying and quantifying the source of noise terms in an observed data set. This method was proposed by David Allan in 1966 (Allan, 1966), and it works in the time domain. The Allan variance is estimated as:

$$\sigma^2(T) = \frac{1}{2T^2(N-2n)} \sum_{k=1}^{N-2n} (\theta_{k+2n} - 2\theta_{k+n} + \theta_k)^2 \qquad (2\text{-}1)$$

where T is the correlation time, or cluster time, it is the time of a group of n consecutive data samples. N is the total number of data samples and θ is the measurement, for the case of an accelerometer it corresponds to the velocity and for the gyro it corresponds to the angle. The sensor measurements are discrete.

To apply the AV method, data is taken for a long period of time (3 hours or more) from a static sensor to get a big number of samples N. The sensor data is integrated to obtain θ. Consecutive data samples are grouped by n samples with a time lapse of T, which is the time difference between the last and the first sample of a group, then formula (2-1) is applied. Later a bigger group of consecutive samples are taken and so on, this is performed until the number of consecutive samples reaches N/2. The AV is plotted in a log-log graph of $\sigma(T)$ versus T, where the slope of certain sections in the graph will indicate the presence of specific noise terms. This is shown in Figure 4. These noise terms are described in Appendix C.

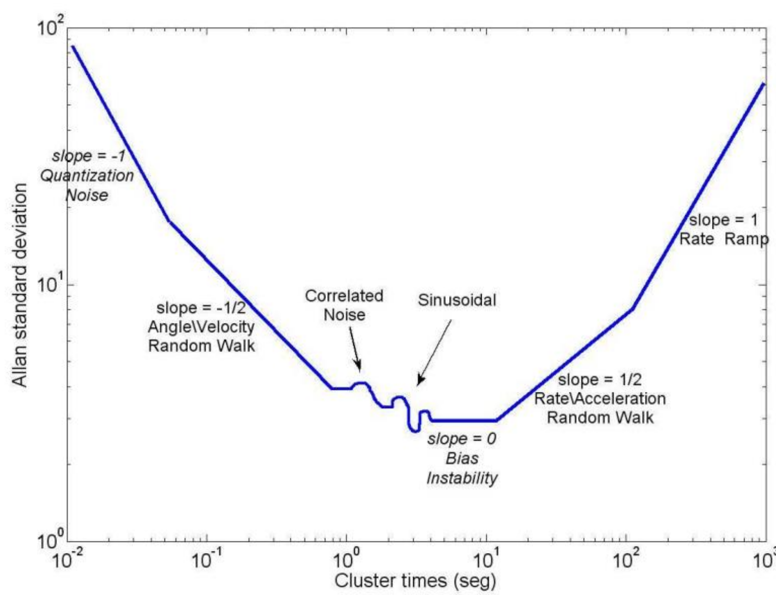

Figure 4. Hypothetical Allan variance graph plot (image taken from IEEE Std 952-1997)

2.3 Magnetometers and Their Calibration

Misalignment, scale factors and biases are also present in magnetometers, but these errors are usually calibrated in the factory. A magnetometer can also be affected by “hard iron” and “soft iron” errors. Hard iron error is produced by the effect of static magnetic fields generated by materials that are permanently close to the magnetometer. Soft Iron errors are produced by permanent materials in the vicinity of the magnetometer that disturb the magnetic field (Wu et al., 2020). The correction model to reduce these errors can be expressed by:

$$\boldsymbol{H} = \boldsymbol{K}^{-1}\boldsymbol{H}_d - \boldsymbol{\beta} \tag{2-2}$$

where $\boldsymbol{H} = [H_x\ H_y\ H_z]^T$ are the magnetometer measurements, $\boldsymbol{H}_d = [H_{dx}\ H_{dy}\ H_{dz}]^T$ represents the ideal measurement, $\boldsymbol{\beta} = [\beta_x\ \beta_y\ \beta_z]^{\boldsymbol{T}}$ is the “Hard iron” error, and $\boldsymbol{K}$ Is the “Soft iron” error.

The “Hard Iron” error produces a displacement away from the magnetometer origin. The “Soft Iron” error scales the measurements a certain amount.

The calibration of the magnetometer starts by taking measurements while rotating the magnetometer around the *x*, *y*, or *z* axis, without moving it from its origin. A 3-D plot of the magnitude vectors produced from the measurements should form a sphere because the magnitude of the magnetic field should be the same at the same point. The reality is that these measurements are noisy and might form an ellipsoid or a deformed ellipsoid instead. Fitting an ellipsoid to the noisy measurements should give the necessary parameters to transform the ellipsoid into a sphere.

The authors in (Wu et al., 2020) proposed to first fit a sphere to the calibration measurements by using the Levenberg-Marquardt (L-M) algorithm. Once the sphere is estimated, the L-M algorithm will be used on a second step by taking the sphere as an initial approximation, but this time it will fit an ellipsoid instead. The resulting ellipsoid contains the parameters that will produce the best estimate of the “Hard Iron” and “Soft Iron” errors.

The L-M algorithm is used to solve the minimum value problem for the sum of squares of functions and has the advantage of using the steepest descent method and the Newton method. The L-M algorithm for magnetometer calibration is described in Appendix D.

2.4 Navigation Coordinate Frames

Cartesian coordinate frames are used for navigation as it allows to locate an object precisely. There are various coordinate frames, the ones described in this section are the body-frame (b-frame), the Local Level Frame (LLF) and the Earth-Centered Earth-Fixed (ECEF).

The body frame is the frame of the moving platform, and the sensors axis are aligned to it. The origin of the b-frame is located at the center of mass of the moving platform. The x-axis of the sensor is aligned to the forward direction, the y-axis of the sensor is aligned with the transversal direction (either left or right) and the z-axis is aligned with the vertical direction following the right-hand rule.

The local level frame (LLF or l-frame) center is at the origin of the sensor, its x-axis points East, its y-axis points to true North and the z-axis points Up. The LLF is also called the navigation frame (n-frame), this frame is shown in Figure 5 below.

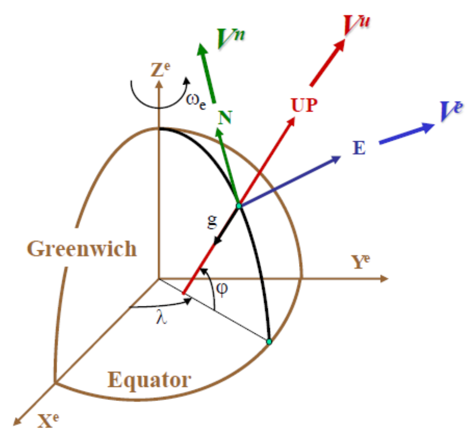

Figure 5. The local level frame (l-frame). East, North and Up (El-Sheimy, Lecture notes 2016)

The ECEF frame origin is located at the center of mass of the Earth. The x-axis points towards the Greenwich meridian and intersects it at the Earth's equatorial plane. The z-axis is aligned with the Earth's polar axis. The y-axis is perpendicular to the x and z-axes, following the right-hand rule. This frame is also called the e-frame. The ECEF rotates with the Earth whose rotation rate is about 15 degrees per hour.

2.5 Chapter Summary

All the sensors used for navigation have their advantages and disadvantages. These sensors also have many errors that adversely affect the quality of the measurements. Some of the errors are deterministic and can be easily removed. The process of removing deterministic errors is done by calibration. Other errors are random in nature, this means that an error at a given time has nothing to do with a previous error. These errors cannot be completely removed but only mitigated. The process to mitigate these random errors is called Stochastic Modelling. To be able to do stochastic modelling, the random process that best suits the error must be identified first. To identify the random process the method of Allan variance is used. This method works in time domain, and it is easier to understand than the methods that work in frequency domain.

It is very important to know the different coordinate frames used in navigation. The body frame (b-frame) is the coordinate system of the moving platform. The origin of the b-frame is located at the center of mass of the moving object. The local level frame (LLF) origin is located at the origin of the inertial sensor. The earth-centered earth-fixed (ECEF) origin is located at the center of mass of the earth, and it rotates along with the earth. The ECEF locates the moving platform in real world coordinates.

Chapter 3: MULTI-SENSOR FUSION AND ALGORITHM DESIGN

Inertial navigation systems (INS) use the dead reckoning method which is very sensitive to the inertial sensor errors. These errors deteriorate the accuracy of the position and attitude very quickly. Adding other sensors to the inertial sensors, can help mitigating these errors by providing complementary information. Adding multiple sensors to improve the accuracy and consistency of a system is called multi-sensor fusion. Integrating information from different sources is called data-fusion.

Algorithms to compute the Allan variance, Magnetometer calibration, the Six static test and the Kalman filter were all implemented in MATLAB.

3.1 Multi-Sensor Fusion

A single sensor it is not capable of measuring all the required information of a system, and each sensor has its own advantages and disadvantages. The idea of multi-sensor fusion is to use each sensor's advantage to improve the overall performance of the system. The sensors advantages and errors for accelerometer, gyroscope and magnetometers are summarized below:

- Accelerometers:

  Provides linear acceleration, gravity vector, velocity, position.

  Errors: Bias, Scale Factor, Misalignment, Noise.

- Gyroscopes:

  Provides angular velocity, attitude.

  Errors: Bias, Scale Factor, Misalignment, Noise

- Magnetometer:

  Provides magnetic field intensity, heading, velocity.

  Errors: Soft Iron, Hard Iron, Noise

The sensor fusion proposed for this research involves the use of accelerometers, gyroscopes, and magnetometers. These sensors will be paired this way:

- Accelerometer – Gyroscope: Provide the necessary information to the mechanization equations.
- Accelerometer - Magnetometer: Both can provide velocity measurements.

These two, will provide the updates to the Kalman Filter for the error state estimation.

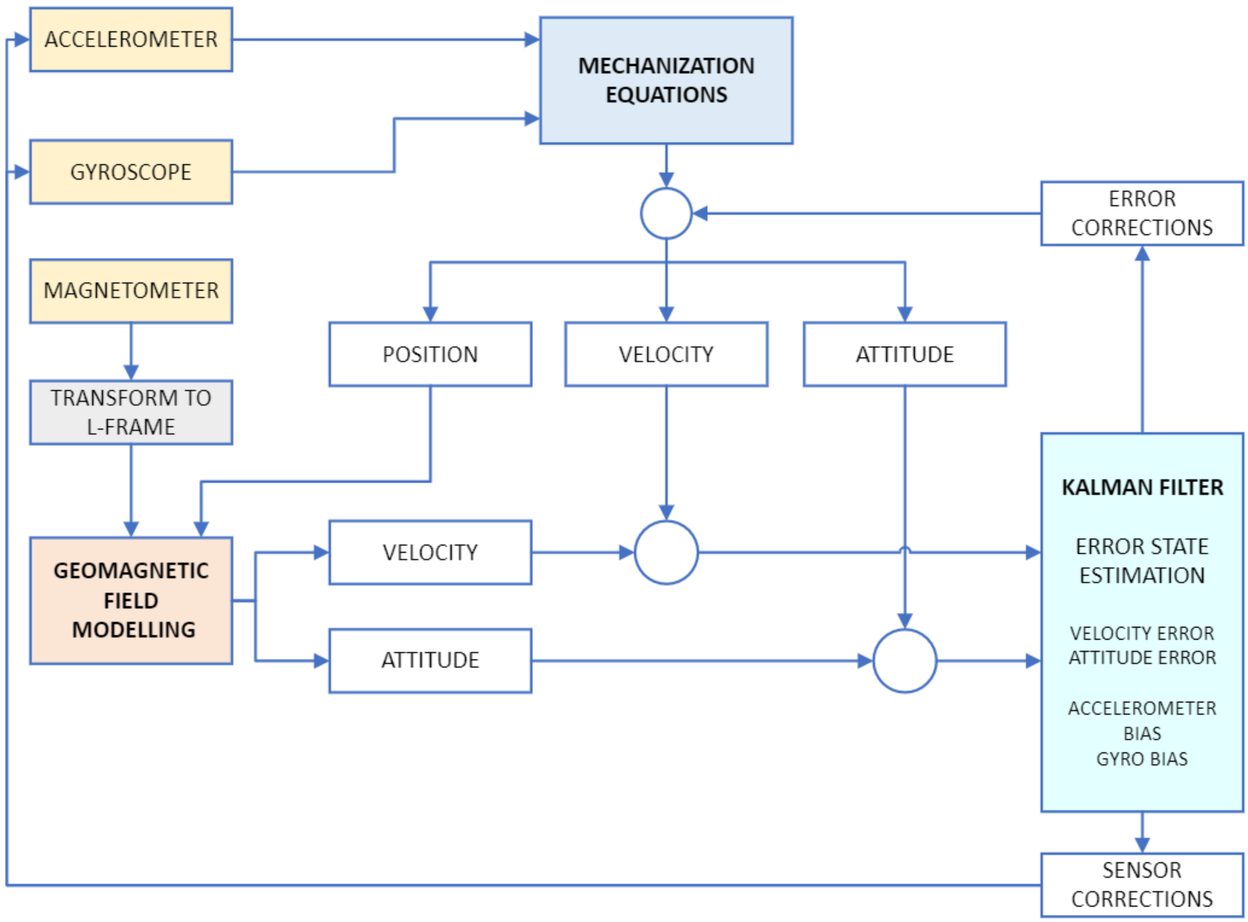

Figure 6. Proposed strapdown INS and Magnetometer Fusion

The Kalman filter in Figure 6. shows the proposed configuration, where the geomagnetic field is measured in the b-frame and transformed to the l-frame, then by modelling the geomagnetic field, attitude and velocity can be estimated and used as an independent measurement that will be fed to the Kalman Filter for error estimation and correction.

3.2 Kalman Filtering

In section 2.4 it was shown that sensors have constant and variable random errors that can't be removed entirely but only mitigated. When these errors enter the mechanization equations, these errors are magnified because of the integration, and this deteriorates the accuracy quickly with time. These errors are called systematic errors. Systematic errors can be reduced by using external measurements by updating the system regularly. The process of using other source of measurements can greatly help to improve the accuracy of the system. The process of joining multiple data sources is called data fusion.

There are various methods to estimate systematic errors, Kalman Filtering (KF) is one of them. The purpose of the KF is to optimally estimate the error states of a system, by using noisy measurements of the system. The KF is a recursive algorithm to solve a linear quadratic estimation problem. It estimates the state of a linear dynamic system corrupted with random white noise, by using measurements that are linearly related to the state, and these measurements are also corrupted by white noise. The KF can work with continuous or discrete time data.

The discrete KF process model is given by:

$$\boldsymbol{X}_k = \boldsymbol{\Phi}_{k-1}\boldsymbol{X}_{k-1} + \boldsymbol{G}_{k-1}\boldsymbol{w}_{k-1} \tag{3-1}$$

where:

$\boldsymbol{X}_k$ is the state vector at time k

$\boldsymbol{\Phi}_{k-1}$ is the state transition matrix at previous time $k-1$

$\boldsymbol{G}_{k-1}$ is the noise coefficient matrix at previous time $k-1$

$\boldsymbol{w}_{k-1}$ is the system noise at previous time $k-1$

The assumptions for the process model of the KF, is that the process noise is white noise, and it is time uncorrelated. This is expressed by these two equations:

$$E\{\boldsymbol{w}_k\} = 0 \tag{3-2}$$

$$E\{\boldsymbol{w}_k\boldsymbol{w}_i^T\} = \begin{cases} \boldsymbol{0}, i \neq k \\ \boldsymbol{Q}_{k,} i = k \end{cases} \tag{3-3}$$

where E is the expectation operator and $\boldsymbol{Q}_{k,}$ is the covariance matrix of the process noise.

The discrete KF measurement model is given by:

$$\boldsymbol{Z}_k = \boldsymbol{H}_k \boldsymbol{X}_k + \boldsymbol{n}_k \tag{3-4}$$

where:

$\boldsymbol{Z}_k$ are the measurements at time k

$\boldsymbol{H}_k$ is the design matrix at time k

$\boldsymbol{X}_k$ error state at time k

$\boldsymbol{n}_k$ is the measurement noise at time k

The assumptions for the measurement model of the KF, is that the measurement noise is white noise, and it is time uncorrelated. This is expressed by these two equations:

$$E\{\boldsymbol{n}_k\} = 0 \tag{3-5}$$

$$E\left\{\boldsymbol{n}_k \boldsymbol{n}_i^{\boldsymbol{T}}\right\} = \begin{cases} \boldsymbol{0}, i \neq k \\ \boldsymbol{R}_{k,}\ i = k \end{cases} \tag{3-6}$$

where $\boldsymbol{R}_{k,}$is the covariance matrix of the process noise.

The other assumption is that the KF requires that the process and measurement noises are uncorrelated between them and uncorrelated with the state vector. This is expressed by:

$$E\left\{\boldsymbol{w}_k \boldsymbol{n}_i^{\boldsymbol{T}}\right\} = 0 \tag{3-7}$$

The last assumption of the KF is that the initial state has a known unbiased estimation $\boldsymbol{x}(t_0)$ and covariance matrix $\boldsymbol{P}_0$, this is expressed by the next two equations:

$$E\{\widehat{\boldsymbol{x}}_0\} = \boldsymbol{x}(t_0) \tag{3-8}$$

$$E\left\{\widehat{\boldsymbol{x}}_0 \widehat{\boldsymbol{x}}_0{}^{\boldsymbol{T}}\right\} = \boldsymbol{P}_0 \tag{3-9}$$

3.3 Kalman Filter Design

Inside the wellbore, there is no GNSS signal, and the only available external aid is the measured depth, which is obtained by adding the length of each drill pipe introduced into the well path. When using the dead reckoning method, this information is not good enough to estimate the attitude and the position, and without any corrections the accuracy deteriorates rapidly with time.

A linear Kalman filter (LKF) was initially chosen, but it didn't provide satisfactory results. The extended Kalman filter was evaluated, and it proved to be better for the tests performed. The Extended Kalman Filter equation summary can be found in Appendix E. The extended Kalman filter will help with the magnetometer's heading estimation and velocity obtained from the magnetometer. To make things simpler the state vector is only composed by 5 state values, and it will only work on a two-dimensional plane:

$$\boldsymbol{x} = [P_E, P_N, H, V_E, V_N]^T \tag{3-10}$$

where

P_E, P_N: Represents the position in the Eastings and the Northings.

H: Represents the sensor's Heading.

V_E, V_N: Represents the velocities in the east and north directions.

The system equations of motion with non-linear dynamics in the discrete Kalman filter are given by:

$$\begin{bmatrix} P_E \\ P_N \\ H \\ V_E \\ V_N \end{bmatrix} = \begin{bmatrix} P_E \\ P_N \\ H \\ V_E \\ V_N \end{bmatrix}_{K-1} + \Delta t * \begin{bmatrix} V_{k-1} * cos(H_{k-1}) \\ V_{k-1} * sin(H_{k-1}) \\ \dot{H} \\ \dot{V}_E \\ \dot{V}_N \end{bmatrix} \tag{3-11}$$

where

$\dot{H}$: Represents the time derivative of the heading.

$\dot{V}_E, \dot{V}_N$: Represents the acceleration in the east and north directions.

The process model state Jacobian matrix obtained by the derivation of (4-7) with respect to each of the state variables is:

$$\boldsymbol{\nabla F_X} = \begin{bmatrix} 1 & 0 & -\Delta t * V_{k-1} * sin(H_{k-1}) & \Delta t * cos(H_{k-1}) & 0 \\ 0 & 1 & \Delta t * V_{k-1} * cos(H_{k-1}) & \Delta t * sin(H_{k-1}) & 0 \\ 0 & 0 & 1 & 0 & 0 \\ 0 & 0 & 0 & 1 & 0 \\ 0 & 0 & 0 & 0 & 1 \end{bmatrix} \quad (3\text{-}12)$$

The covariance matrix of the state vector $\boldsymbol{P_0}$ is assigned zeros initially:

$$\boldsymbol{P_0} = \begin{bmatrix} 0 & 0 & 0 & 0 & 0 \\ 0 & 0 & 0 & 0 & 0 \\ 0 & 0 & 0 & 0 & 0 \\ 0 & 0 & 0 & 0 & 0 \\ 0 & 0 & 0 & 0 & 0 \end{bmatrix} \quad (3\text{-}13)$$

The covariance matrix of the process noise $\boldsymbol{Q}$ is assigned these values initially:

$$\boldsymbol{Q_0} = \begin{bmatrix} 0 & 0 & 0 & 0 & 0 \\ 0 & 0 & 0 & 0 & 0 \\ 0 & 0 & \Delta t^2 * {\sigma_H}^2 & 0 & 0 \\ 0 & 0 & 0 & \Delta t^2 * {\sigma_a}^2 & 0 \\ 0 & 0 & 0 & 0 & \Delta t^2 * {\sigma_a}^2 \end{bmatrix} \quad (3\text{-}14)$$

where

σ_H: Is the standard deviation for the heading angle.

σ_a: Is the standard deviation for the accelerometer.

The accelerometer's measurement model is given by:

$$\boldsymbol{z_a} = \begin{bmatrix} f_x \\ f_y \end{bmatrix} \quad (3\text{-}15)$$

where

f_x: Is the accelerometer measurement from the *x* axis.

f_y: Is the accelerometer measurement from the *y* axis.

$$\boldsymbol{H_a} = \begin{bmatrix} 0 & 0 & 0 & 1 & 0 \\ 0 & 0 & 0 & 0 & 1 \end{bmatrix} \quad (3\text{-}16)$$

$$\boldsymbol{R_a} = \begin{bmatrix} \sigma^2{}_{a_e} & 0 \\ 0 & \sigma^2{}_{a_n} \end{bmatrix} \quad (3\text{-}17)$$

where

σ_{a_e}: Is the standard deviation for the accelerometer x axis.

σ_{a_n}: Is the standard deviation for the accelerometer y axis.

The magnetometer's measurement model is given by:

$$\boldsymbol{z_{mag}} = \begin{bmatrix} H_{mag} \\ V_{magX} \\ V_{magY} \end{bmatrix} \quad (3\text{-}18)$$

where

H_{mag}: Is the angular rate of change, estimated from harmonic polynomials.

V_{magX}, V_{magY}: Are the estimated velocities from the magnetic field change.

$$\boldsymbol{H_{mag}} = \begin{bmatrix} 0 & 0 & 1 & 0 & 0 \\ 0 & 0 & 0 & 1 & 0 \\ 0 & 0 & 0 & 0 & 1 \end{bmatrix} \quad (3\text{-}19)$$

$$\boldsymbol{R_{mag}} = \begin{bmatrix} \sigma^2{}_H & 0 & 0 \\ 0 & \sigma^2{}_{V_e} & 0 \\ 0 & 0 & \sigma^2{}_{V_n} \end{bmatrix} \quad (3\text{-}20)$$

where

σ_{v_e}: Is the standard deviation for the velocity in the x axis due to a magnetic field change.

σ_{v_n}: Is the standard deviation for the velocity in the y axis due to a magnetic field change.

3.4 Modelling The Physical Magnetic Field

A magnetic field can be described by using vectors at each point in space, and as such it can be treated as a vector field. Each vector represents the forces induced by the field. The field is generated by magnetic minerals or by electric currents. Maxwell equations (Maxwell, 1996) define the physical magnetic field, which states that in the vacuum, the divergence and curl of the magnetic field is zero:

$$\boldsymbol{\nabla} \cdot \boldsymbol{B} = 0 \; and \; \boldsymbol{\nabla} \times \boldsymbol{B} = 0 \qquad (3\text{-}21)$$

In the absence of an electric current, the scalar potential of the magnetic field, obeys Laplace equation:

$$\boldsymbol{\nabla}^{\mathbf{2}} \phi = 0 \qquad (3\text{-}22)$$

There are many solutions to Laplace equation, but there is a well-known set of functions that can solve Laplace equations with boundary constraints. A set of harmonic polynomials of degree *n* and *k* variables was presented in (Miles & Williams, 1955). The harmonic polynomials for 3 variables and 4th order harmonic polynomials to expand the scalar potential of the magnetic field are presented here:

$$\phi = a_0 + xa_1 + ya_2 + za_3 + xya_4 + xza_5 + yza_6 + (x^2 - z^2)a_7 + (y^2 - z^2)a_8 + xyza_9 + (x^3 - 3xz^2)a_{10} + (xy^2 - xz^2)a_{11} + (y^3 - 3yz^2)a_{12} + (x^2y - yz^2)a_{13} + (3x^2z - z^3)a_{14} + (3y^2z - z^3)a_{15} + (x^3y - 3xyz^2)a_{16} + (xy^3 - 3xyz^2)a_{17} + (x^3z - xz^3)a_{18} + (3xy^2z - xz^3)a_{19} + (3x^2yz - yz^3)a_{20} + (y^3z - yz^3)a_{21} + (x^4 - 6x^2z^2 + z^4)a_{22} + (y^4 - 6y^2z^2 + z^4)a_{23} + (3x^2y^2 - 3x^2z^2 - 3y^2z^2 + z^4)a_{24} + \cdots \qquad (3\text{-}23)$$

These polynomials are in fact harmonic as they solve Laplace equation. The parameter a_0 represents the monopole, which for the magnetic field doesn't have a physical meaning and it can be discarded.

From (3-23) we can see there are 24 parameters that need to be solved to expand the harmonic polynomials to a 4th order. These 24 parameters can only be solved for a group of points in space if the magnetic field components are known or measured at each point. The solution of those parameters will fit the magnetic field to the volume enclosed by the group of points. Once the magnetic field is modelled, the field can be estimated at any other point within the vicinity of the known points. The fitting procedure is achieved by minimizing the sum of the squares of the differences, for detailed formula development please refer to (Rodrigo Ramon, 2018).

The gradient of the scalar potential will provide the magnetic field:

$$\boldsymbol{B} = -\boldsymbol{\nabla}\phi \tag{3-24}$$

where:

$$\boldsymbol{B_x} = \frac{\partial \phi}{\partial x} = a_1 + ya_4 + za_5 + 2xa_7 + yza_9 + (3x^2 - 3z^2)a_{10} + (y^2 - z^2)a_{11} + 2xya_{13} + (3x^2y - 3yz^2)a_{16} + (y^3 - 3yz^2)a_{17} + (3x^2z - z^3)a_{18} + (3y^2z - z^3)a_{19} + 6xyza_{20} + (4x^3 - 12xz^2)a_{22} + (6xy^2 - 6xz^2)a_{24} \tag{3-25}$$

$$\boldsymbol{B_y} = \frac{\partial \phi}{\partial y} = a_2 + xa_4 + za_6 + 2ya_8 + xza_9 + 2xya_{11} + (3y^2 - 3z^2)a_{12} + (x^2 - z^2)a_{13} + 6yza_{15} + (x^3 - 3xz^2)a_{16} + (3xy^2 - 3xz^2)a_{17} + 6xyza_{19} + (3x^2z - z^3)a_{20} + (3y^2z - z^3)a_{21} + (4y^3 - 12yz^2)a_{23} + (6x^2y - 6yz^2)a_{24} \tag{3-26}$$

$$\boldsymbol{B_z} = \frac{\partial \phi}{\partial z} = a_3 + xa_5 + ya_6 - 2za_7 - 2za_8 + xya_9 - 6xza_{10} - 2xza_{11} - 6yza_{12} - 2yza_{13} + (3x^2 - 3z^2)a_{14} + (3y^2 - 3z^2)a_{15} - 6xyza_{16} - 6xyza_{17} + (x^3 - 3xz^2)a_{18} + (3xy^2 - 3xz^2)a_{19} + (3x^2y - 3yz^2)a_{20} + (y^3 - 3yz^2)a_{21} + (-12x^2z + 4z^3)a_{22} + (-12y^2z + 4z^3)a_{23} + (-6x^2z - 6y^2z + 4z^3)a_{24} \tag{3-27}$$

These harmonic polynomials can be evaluated on a set of points, usually at grid points:

$$\boldsymbol{P} = [p_1, p_2, p_3, \dots, p_n] \tag{3-28}$$

With the harmonic polynomials in compact form evaluated at a single point p:

$$\boldsymbol{B_x}(p) = \sum_{\mathbf{m=1}}^{\mathbf{24}} a_m\, \boldsymbol{B_x^m}(p) \tag{3-29}$$

$$\boldsymbol{B_y}(p) = \sum_{\mathbf{m=1}}^{\mathbf{24}} a_\mathrm{m}\, \mathbf{B_y^m}(p) \tag{3-30}$$

$$\boldsymbol{B_z}(p) = \sum_{\mathbf{m=1}}^{\mathbf{24}} a_{\mathrm{m}}\, \mathbf{B_z^m}(p) \tag{3-31}$$

Or in general compact form:

$$\boldsymbol{B}_{\mathbf{i}}(p) = \sum_{\mathrm{m=1}}^{24} a_{\mathrm{m}}\, \mathbf{B_i^m}(p) \tag{3-32}$$

where m is to index the harmonic polynomial and, $i = 1, 2,3$ to index the 3 axis, x, y, and z.

If the magnetic field is measured at point p:

$$\overline{\boldsymbol{B}}_{\boldsymbol{i}}(p) = \left[\overline{\boldsymbol{B}}_{\boldsymbol{x}}(p), \overline{\boldsymbol{B}}_{\boldsymbol{y}}(p), \overline{\boldsymbol{B}}_{\boldsymbol{z}}(p)\right] \tag{3-33}$$

The measured field should equal the harmonic polynomials:

$$\overline{\boldsymbol{B}}_{\mathbf{i}}(\mathrm{p}) = \sum_{\mathrm{m=1}}^{24} a_{\mathrm{m}}\, \mathbf{B_i^m}(p) \tag{3-34}$$

The coefficients $a_{\mathrm{m}}$are solved with the least squares method by minimizing the cost function:

$$\boldsymbol{\chi^2} = \sum_{\boldsymbol{i=1}}^{\mathbf{3}} \sum_{\boldsymbol{j=1}}^{\boldsymbol{n}} \left[\frac{\overline{\boldsymbol{B}}_{\mathrm{i}}(p_j) - \sum_{\mathrm{m=1}}^{24} a_{\mathrm{m}} \mathbf{B_i^m}(p_j)}{\boldsymbol{\sigma_{i,j}}}\right]^{\mathbf{2}} \tag{3-35}$$

With j =1, 2, 3, …, number of measured points and $\boldsymbol{\sigma_{i,j}}$ being the standard deviation of the measurements.

The solution of the least squares problem is the matrix equation:

$$\sum_{\mathrm{m=1}}^{24} \propto_{k,m} a_m = \gamma_{\mathrm{k}} \tag{3-36}$$

with $k = 1, \ldots, 24$ and $\propto_{k,m}$ is the 24x24 matrix:

$$\propto_{k,m} = \sum_{\boldsymbol{i=1}}^{\mathbf{3}} \sum_{\boldsymbol{j=1}}^{\boldsymbol{n}} \frac{\mathbf{B_i^m}(p_j)\mathbf{B_i^k}(p_j)}{\boldsymbol{\sigma_{j,i}}^{\mathbf{2}}} \tag{3-37}$$

and γ_{k} is the vector with length 24:

$$\gamma_{\mathrm{k}} = \sum_{\boldsymbol{i=1}}^{\mathbf{3}} \sum_{\boldsymbol{j=1}}^{\boldsymbol{n}} \frac{\overline{\boldsymbol{B}}_{\mathrm{i}}(p_j)\mathbf{B_i^m}(p_j)}{\boldsymbol{\sigma_{j,i}}^{\mathbf{2}}} \tag{3-38}$$

The inverse of matrix $\propto_{k,m}$ is the covariance variance of the estimated parameters a_m:

$$C = \propto^{-1} \quad (3\text{-}39)$$

The coefficients $a_{\mathrm{m}}$are equal to:

$$a_m = \sum_{\mathrm{m}=1}^{24} \propto_{k,m}{}^{-1} \gamma_{\mathrm{k}} \quad (3\text{-}40)$$

To solve for the 24 parameters of 4th order harmonic polynomials, at least 8 points with magnetic field measurements are required. Even though with 1 measured point a result can be obtained with the least squares method, it probably is not very accurate. But the solution might be enough for a point close to a measured point (less than 20cm). A magnetometer is constantly taking measurements as the sensor is moving and these can be used to improve the accuracy of the polynomials over time.

To estimate the heading, harmonic polynomials will be estimated at an initial sensor's position, if the sensor moves a small distance away from this initial position, the magnetic field can be extrapolated to the new position, then compared with the actual reading at that position. If there is no change in heading, then the values must be equal or very similar, otherwise a change in heading has occurred and its angular change can be easily determined. This angular change is the relative heading, and when added to the previous heading, the heading at the new position is obtained.

The relationship of the magnetic field measurements in the local level frame and the body frame is given by:

$$\boldsymbol{B}^b = R_l^b \boldsymbol{B}^l \quad (3\text{-}41)$$

where $R_l^b$is the rotation matrix to change from the local level frame l, to the body frame b.

It is assumed that the magnetic field is not changing with time, and this is a good assumption for a short period of elapse time. Because of this assumption, it can also be assumed that the magnetic field is only changing in space. This relationship in the local level frame can be deduced by the chain rule applied to (3-41):

$$\dot{\boldsymbol{B}}^l = J^l(\boldsymbol{B})\boldsymbol{V}^l \tag{3-42}$$

where $\boldsymbol{V}^l$ is the velocity in the local level frame and $J^l(\boldsymbol{B})$, is the Jacobian of the magnetic field:

$$J(\boldsymbol{B}) = \begin{bmatrix} \frac{\partial B_x}{\partial x} & \frac{\partial B_y}{\partial x} & \frac{\partial B_z}{\partial x} \\ \frac{\partial B_x}{\partial y} & \frac{\partial B_y}{\partial y} & \frac{\partial B_z}{\partial y} \\ \frac{\partial B_x}{\partial z} & \frac{\partial B_y}{\partial z} & \frac{\partial B_z}{\partial z} \end{bmatrix} \tag{3-43}$$

The rate of change of the magnetic field is better expressed in the body frame (where the measurements are taken):

$$\dot{\boldsymbol{B}}^b = -\boldsymbol{\Omega} \times \boldsymbol{B}^{\boldsymbol{b}} + J^b(\boldsymbol{B})\boldsymbol{V}^b \tag{3-44}$$

where $\boldsymbol{\Omega}$, is the rate of rotation coming from the gyroscope.

Usually, 4 or 3 magnetometers are used to find the gradients of the magnetic field, but this thesis will only use one 3-axis magnetometer, and to obtain the gradients the harmonic polynomials will be used.

3.5 Chapter Summary

It has been proven that fusing information coming from multiple sensors that are measuring a process has many more benefits than using each sensor information separately. The benefits of data fusion are that it produces information obtained from the process which is more consistent and more accurate than the actual raw data coming from each source. In most of the cases one single sensor cannot measure what is required to be measured from a system, so other sensors need to be added. Taking information from multiple sensors is called multi-sensor fusion. The Kalman filter is a recursive optimal estimator that has many applications and can be used to fuse sensor data. The Kalman filter assumes linear dynamics and gaussian distributions. For the cases of a non-linear system the extended Kalman filter can be used as it uses a first-order approximation around the state and covariance at a certain point in time.

Harmonic polynomials were introduced in this chapter. They follow the physical properties of the magnetic field. Because the magnetic field is a potential field the Laplace equation is equal to zero. One of the many possible solutions for the Laplace equation are the harmonic polynomials. The coefficients of the harmonic polynomials must be solved to be able to use them. This was done by defining and minimizing the cost function.

Chapter 4: METHODS

The sensor used to evaluate and test the methods presented in the previous chapters was the Analog Device ADIS16448 sensor. This sensor has a triaxial digital gyroscope, a triaxial digital accelerometer, and a triaxial magnetometer (Analog-Devices, n.d.). Table 1 shows the sensor specifications. The magnetometer measurements of the magnetic flux density are in Gauss, the equivalent to the SI unit of a Gauss is:

$$1\ Gauss \approx 10^{-4} Tesla = \ 10^{-4} \frac{Kg}{A \cdot s^2}$$

Table 1. ADIS16448 Sensor specifications

(https://www.analog.com/media/en/technical-documentation/data-sheets/adis16448.pdf)

Accelerometer	Dynamic range: ±18 g Sensitivity: 0.833 mg/LSB Bias Repeatability: 20 mg Noise density: 0.23 m$g/\sqrt{Hz}$ rms Misalignment axis to-axis: 0.2 Degrees Velocity Random Walk: 0.11 m/sec/√hr Operating temperature: -40℃ ~ +85℃
Gyroscope	Dynamic range: ±1200 deg/s Initial Sensitivity: 0.04 °/sec/LSB Rate noise density: 0.0135 °/sec/√Hz rms Output noise: 0.27 degree/second rms Misalignment axis to-axis: ±0.05 Degrees Angular Random Walk: 0.66 °/√hr Operating temperature: -40℃ ~ +85℃
Magnetometer	Dynamic range: ±1.9 Gauss Initial Sensitivity:142.9 μGauss/LSB Misalignment Axis to axis:0.25 Degrees Noise Density: 0.4 mGauss/√Hz Output Noise: 2.4 mGauss Operating temperature: -40℃ ~ +85℃

Static data were collected at the U of C G12 lab, for the analysis of deterministic and random errors that affect the accelerometers and the gyroscopes, and to calibrate the magnetometer.

4.1 Inertial Sensors Calibration

To find the inertial sensors bias and scale factors, the six-position method was used. Sensor readings were taken for 30 minutes for each axis in the Up and Down. The bias and scale factor for each of the accelerometer axes can be found by:

$$\text{Bias}_f = \frac{Up_f + Down_f}{2} \tag{4-1}$$

$$\text{Scale Factor}_f = \frac{Up_f - Down_f - 2g}{2g} \tag{4-2}$$

where g can be computed from the normal gravity formula that can be found in Appendix A.

The bias and scale factor for each of the gyroscope axes can be found by:

$$\text{Bias}_\omega = \frac{Up_\omega + Down_\omega}{2} \tag{4-3}$$

$$\text{Scale Factor}_\omega = \frac{Up_\omega - Down_\omega - 2\omega_e sin\varphi}{2\omega_e sin\varphi} \tag{4-4}$$

where $\omega_e$is the Earth's rotation rate and φ is the latitude.

The results for the ADIS16448 accelerometers and gyroscopes are given in Table 2.

Table 2. Six position tests for the calibration of ADIS16448 accelerometers and gyroscopes

Sensor	Bias Offset	Scale Factor
Accelerometer X	0.0487 m/s^2	-0.0019
Accelerometer Y	-0.0081 m/s^2	-0.0020
Accelerometer Z	0.0394 m/s^2	-0.0020
Gyroscope X	-0.0278 deg/s	3.4761
Gyroscope Y	-0.3783 deg/s	2.4835
Gyroscope Z	0.1823 deg/s	-5.6840

4.2 Allan Variance

Static data was collected in the U of C G12 lab, for 3 hours for analysis of the random errors that affect the accelerometers and the gyroscopes of the ADIS16448 sensor. The sensor was set to a sampling frequency of 12.8 Hz.

Figure 7 shows a log-log plot of the cluster time versus the Allan variance for the ADIS16448 three axis accelerometer.

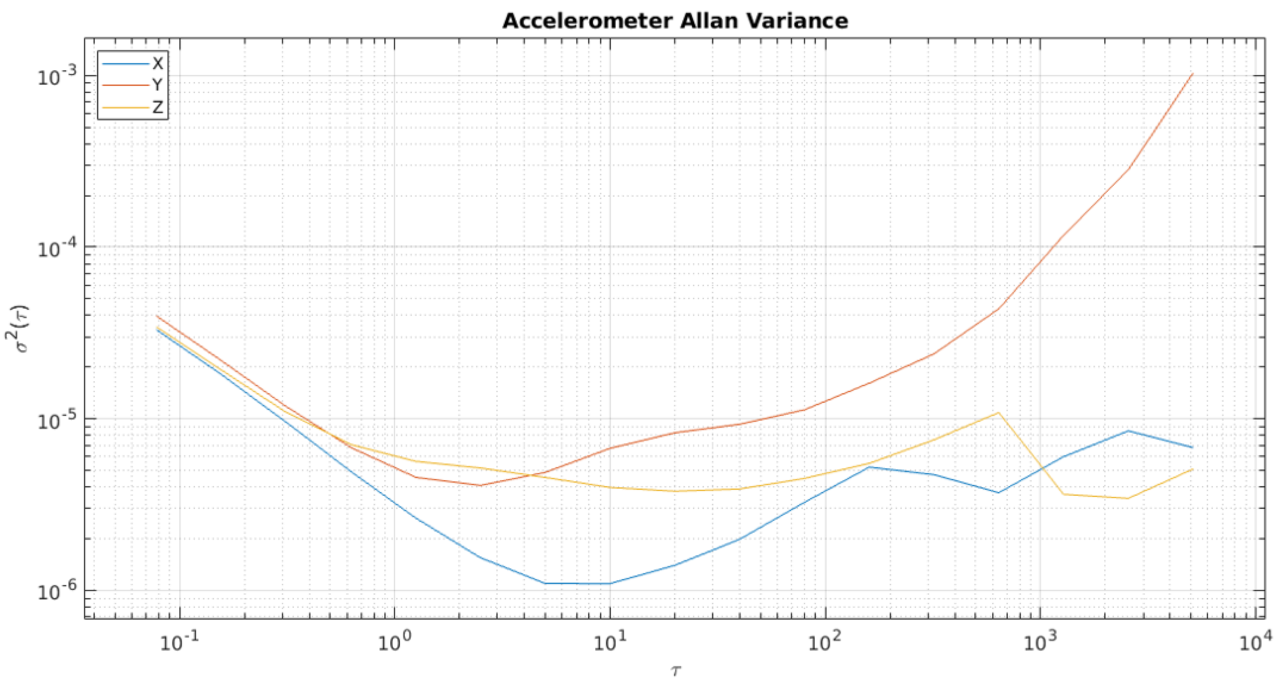

Figure 7. ADIS16448 Accelerometer Allan variance log-log plot results

The results in Table 3 shows that the dominant noises of the accelerometers are the velocity, acceleration random walk and the bias instability.

Table 3. ADIS16448 Accelerometer noise coefficients from Allan variance

Sensor	**Quantization Noise** m/s^2	**Velocity Random Walk** $m/s/\sqrt{h}$	**Bias Instability** m/s^2	**Acceleration Random Walk** $m/s/h^{3/2}$	**Rate Ramp** $m/s/h^2$
Accelerometer X	0.0	1.727E-03	1.576E-03	3.857E-04	0.0
Accelerometer Y	0.0	1.845E-03	3.213E-03	4.732E-04	9.2840E-06
Accelerometer Z	0.0	1.636E-03	2.927E-03	0.0	0.0

Figure 8, Figure 9, and Figure 10 shows how lines with the slopes of -1, 0, and 1 fitted to the log-log plot of the cluster time versus the Allan variance to find the coefficients for the respective noises.

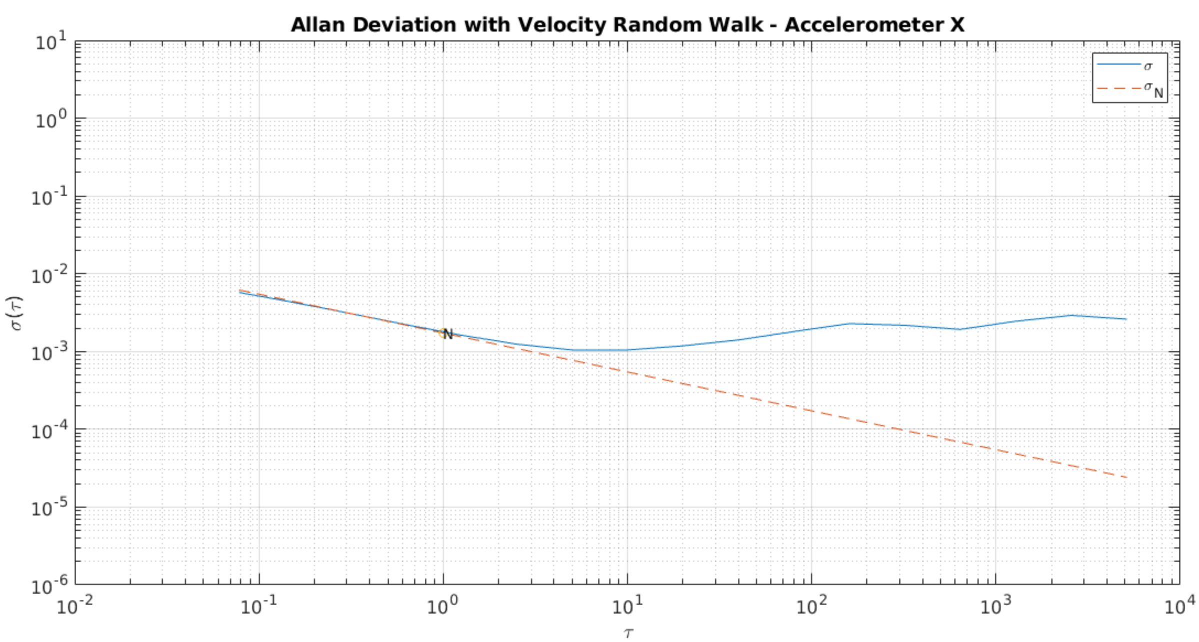

Figure 8. Velocity random walk (N) is found by fitting a line with a slope of -1 to the log-log plot.

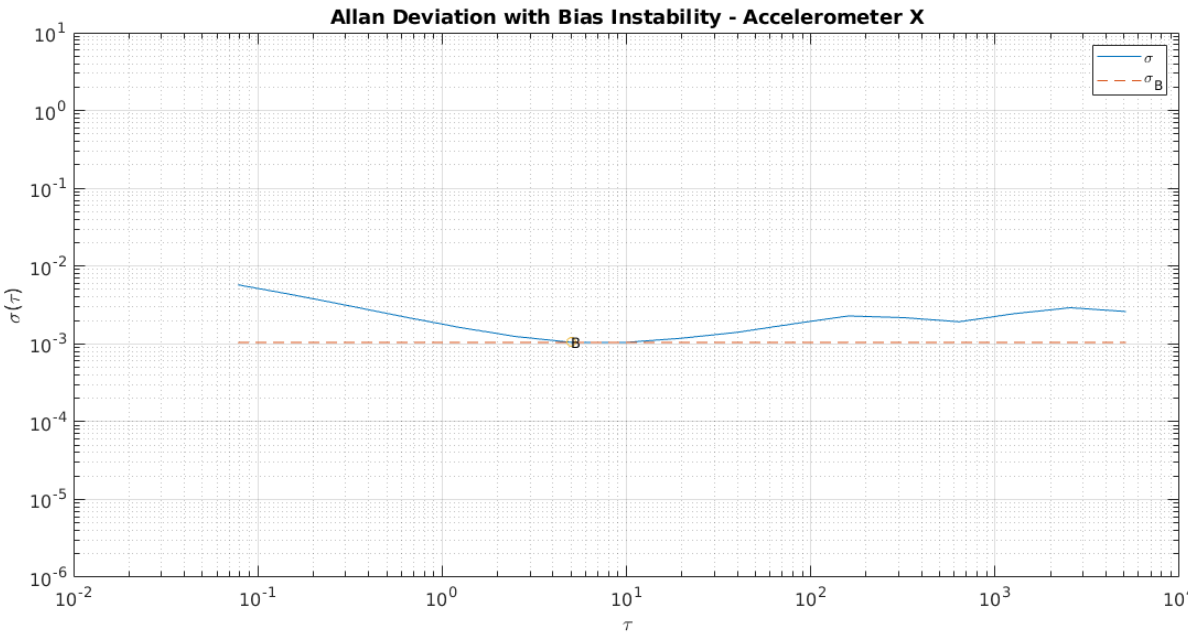

Figure 9.Bias Instability (B) is found in the log-log plot by fitting a line with a slope of 0.

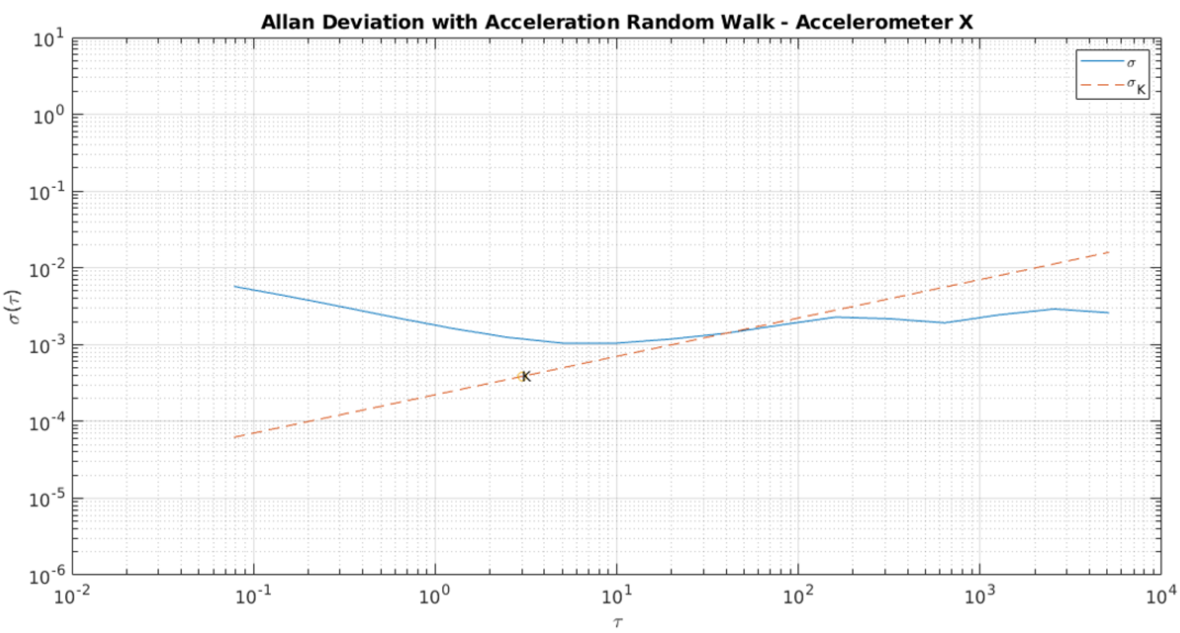

Figure 10.Accelerometer random walk (K) is found in the log-log plot by fitting a line with a slope of +1

Figure 11 shows the log-log plot of the cluster time versus the Allan variance for the ADIS16448 three axis gyroscope.

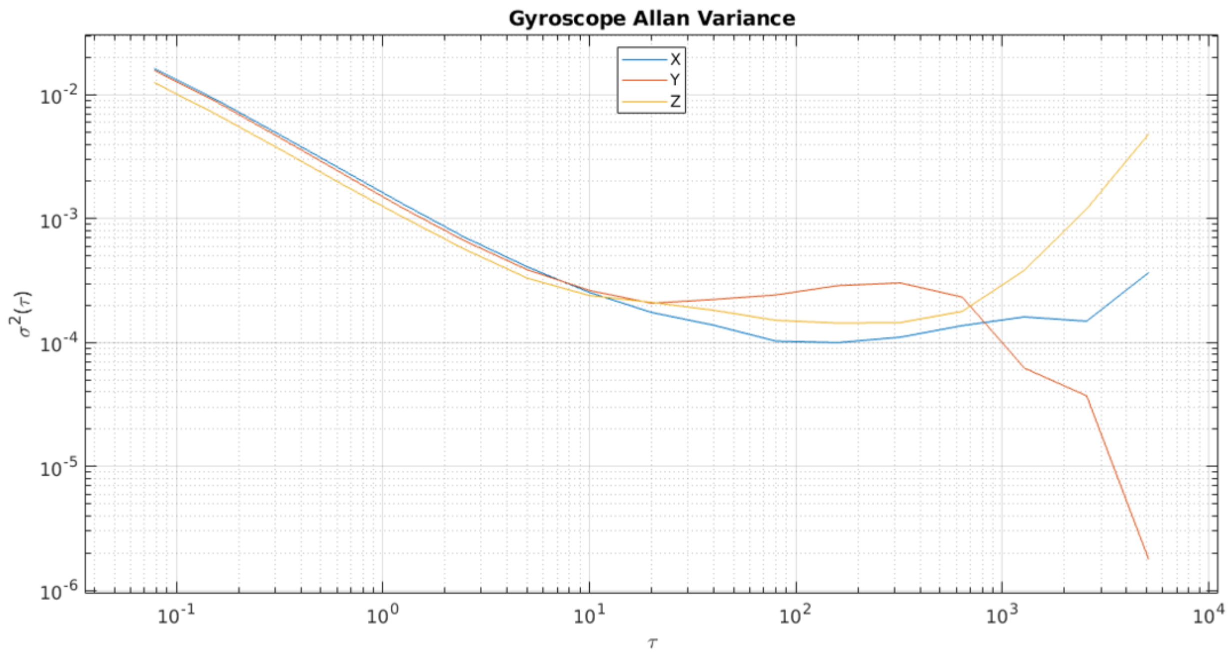

Figure 11.ADIS16448 Gyroscope Allan variance log-log plot

The results in Table 4 shows that the dominant noises of the gyroscopes are the angle random walk, rate random walk and the bias instability.

Table 4. ADIS16448 Accelerometer noise coefficients from Allan variance

Sensor	**Quantization Noise** deg	**Angle Random Walk** $deg/\sqrt{h}$	**Bias Instability** deg/h	**Rate Random Walk** $deg/h^{3/2}$	**Rate Ramp** deg/h^2
Gyroscope X	0.0	3.970E-02	1.527E-02	4.178E-04	0.0
Gyroscope Y	5.6	3.780E-02	2.559E-02	0.0	0.0
Gyroscope Z	0.0	3.395E-02	1.806E-02	9.155E-04	1.912E-05

Figure 12, Figure 13 and Figure 14 shows how lines with the slopes of -1, 0, and 1 are fitted to the log-log plot of the cluster time versus the Allan variance to find the coefficients for the respective noises.

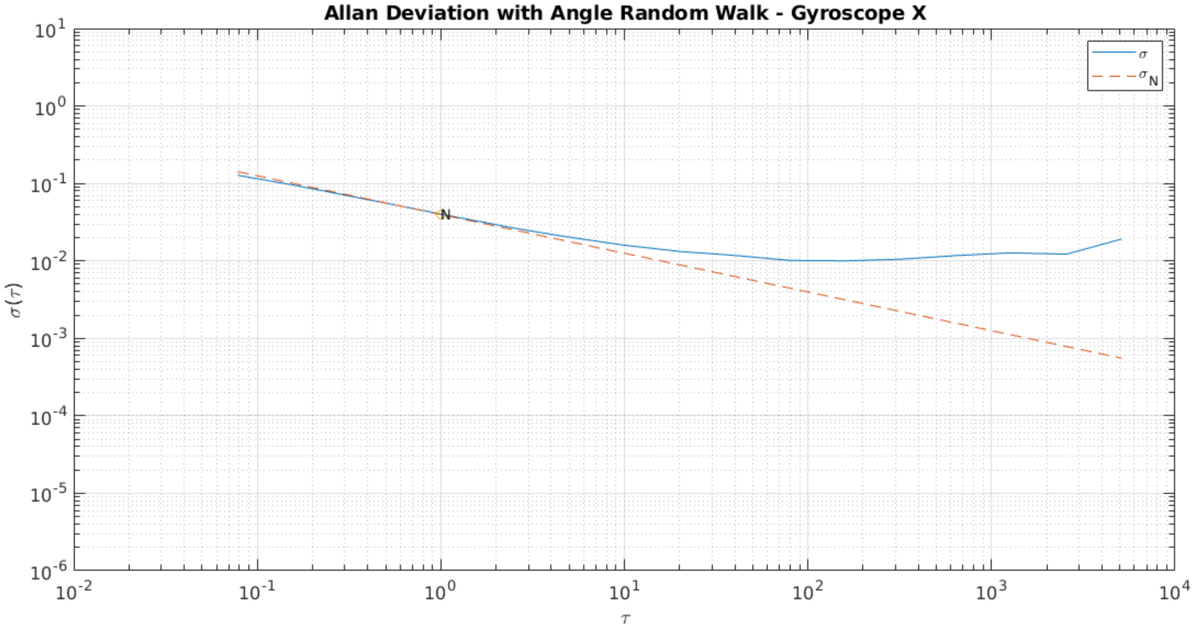

Figure 12. Angle random walk (N) is found by fitting a line with a slope of -1 to the log-log plot

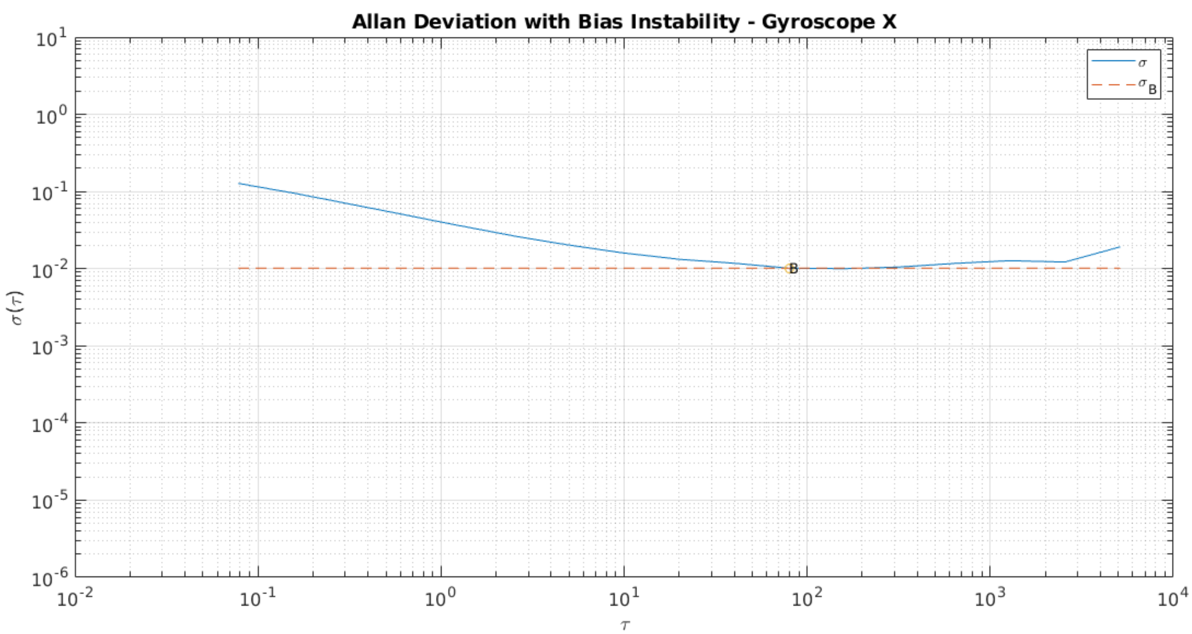

Figure 13.Bias Instability (B) is found in the log-log plot by fitting a line with a slope of 0

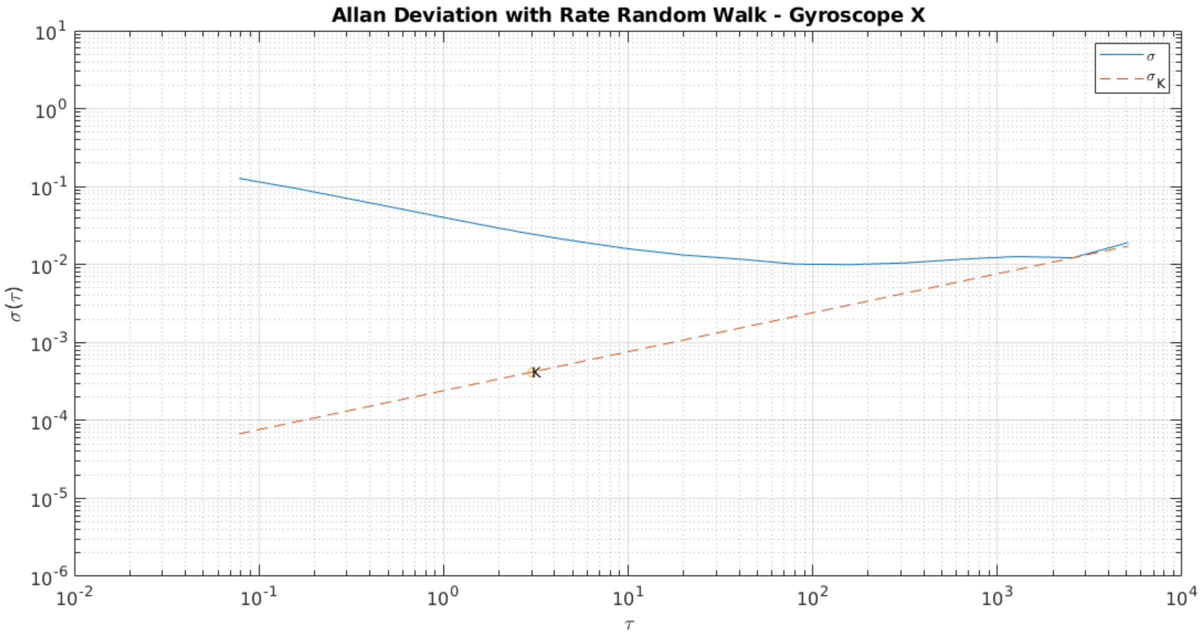

Figure 14. Rate random walk (K) is found in the log-log plot by fitting a line with a slope of +1

4.3 Magnetometer Calibration

Static data was collected at the U of C G12 lab, to be used for the calibration of the magnetometer. The ADIS16448 sensor was rotated every 30° to complete a 360° rotation around each of its axes. Magnetometer measurements were taken at each station for 30 seconds. The data taken in this way would not form a sphere (as desired), but it will define two parallel circles one at the north and the other at the south of the sphere.

The LM-Algorithm was initially used to fit a sphere to the measurements and to calculate the hard iron error β which is equal to the coordinates of the center of the sphere that best fits the measurements. The sphere and the hard iron errors were then fed to the LM algorithm as a second step to best fit an ellipsoid. This ellipsoid will measure the amount by which the sphere is deformed by the effect of the soft iron errors.

Table 5. Estimated Hard and Soft Iron errors for the ADIS16448 magnetometer

Sphere Radius (Magnetic Field Intensity)	41.2985212568177 µTesla
Hard Iron Error ($\boldsymbol{\beta}$) (µTesla)	[-0.7434420435, 1.013726925, -0.0728716243]
Soft Iron Error (**K**)	$\begin{bmatrix} 0.999999788 & -6.17E^{-07} & 1.13E^{-05} \\ -6.17E^{-07} & 1.00000003 & -3.12E^{-07} \\ 1.13E^{-05} & -3.12E^{-07} & 0.999995143 \end{bmatrix}$

It can be seen from the results shown in Table 5 that the hard iron errors are small, and the soft iron error are also very small, this might be since the sensor was not affected by other magnetic parts attached to it. Figure 15, Figure 16, Figure 17, and Figure 18 show the sphere and ellipsoid final fit to the ADIS16448 magnetometer.

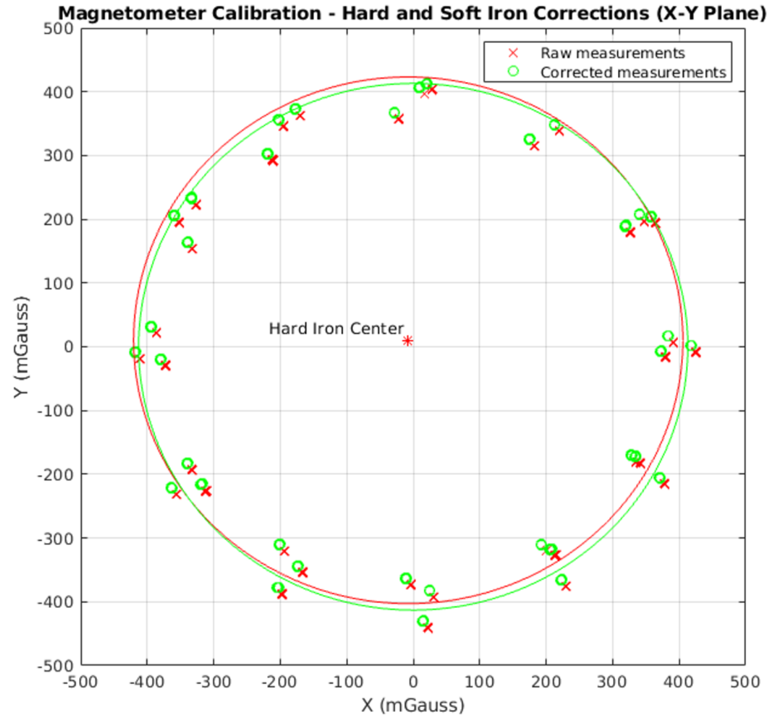

Figure 15. Sphere fit projection on the X-Y plane represented by the red circle.

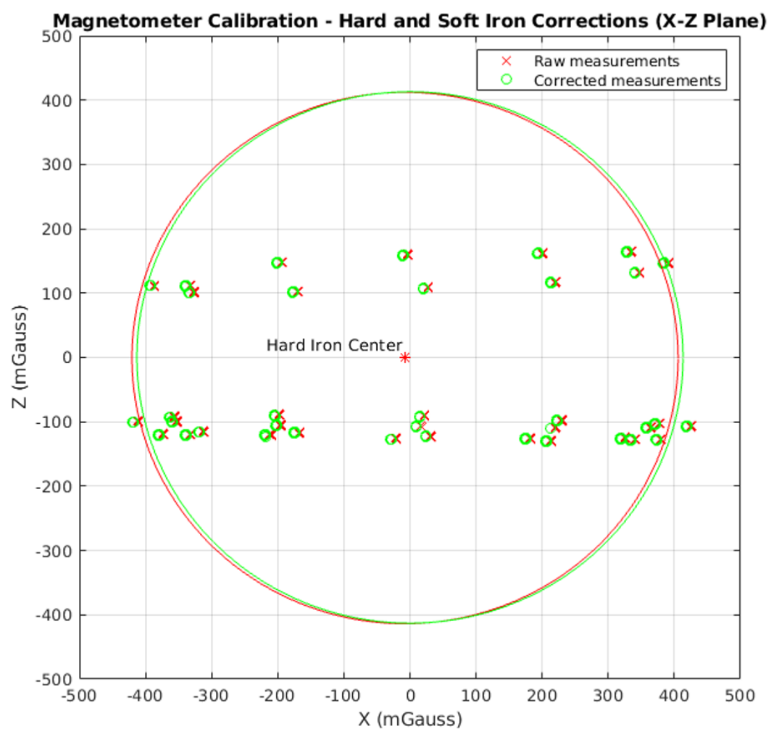

Figure 16. Sphere fit projection on the X-Z plane represented by the red circle.

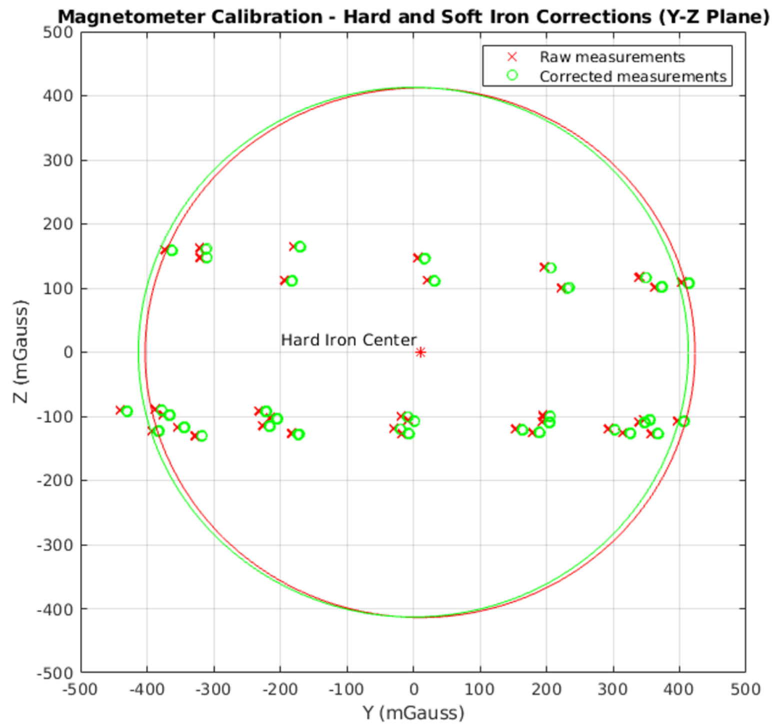

Figure 17. Sphere fit projection on the Y-Z plane represented by the red circle

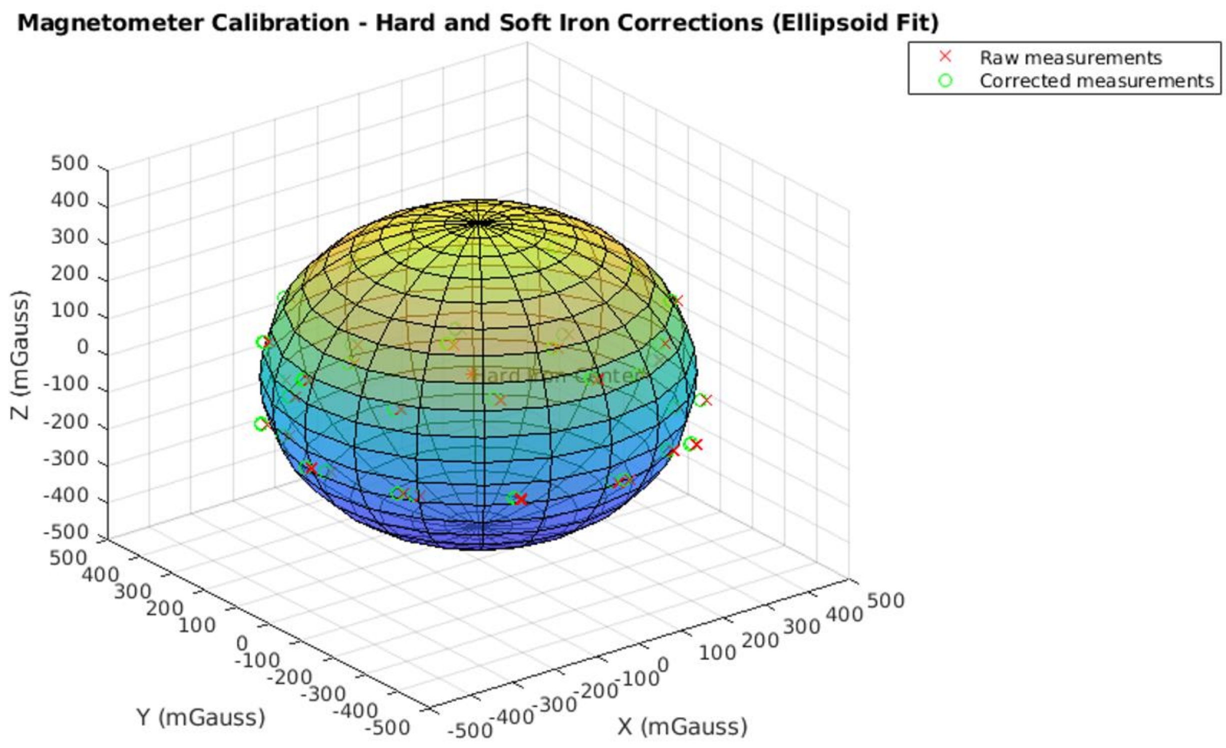

Figure 18. Sphere fit to the measurements 3-D Plot

4.4 Chapter Summary

The six-position method was applied to calibrate the accelerometers and gyroscopes. These results were applied to the raw measurements when used on the tests described in the following chapters.

To identify some of the random errors present in each axis of the accelerometer and the gyroscope, 3 hours of static measurements were taken. The Allan variance was calculated by using the function available for it in MATLAB. These random errors seemed to be very small and were not modelled in the extended Kalman filter.

The magnetometer was also calibrated by rotating the sensor on each of its axis and by taking measurements at each rotation. This process is very complicated as the sensor's origin point should ideally be kept at the same location. All the rotations together should take the form of a 3D-sphere. The soft and hard iron errors obtained from this calibration were corrected on each of the magnetometer raw measurements taken on the tests described in the following chapters.

Chapter 5: TEST SETUP AND PERFORMANCE ANALYSIS

5.1 Test Setup

A 6.6 by 6.6 m grid has been created in the University of Calgary Engineering G12 laboratory floor with a grid spacing of 0.60 m, forming a total of 144 grid points. With the intention of making a map of the magnetic field at the lab's floor level, the ADIS16448 sensor was used collect magnetic field measurements at each grid point position. The map will show if there are magnetic anomalies present and their location.

Of particular interest for this thesis, is to find out if it is possible to estimate relative heading in the presence of magnetic anomalies. To evaluate this, two types of tests were performed, one with a static sensor (sensor not moving) and the second one with the sensor moving on a railing track.
A rail track shown in Figure 19, was also set up in G12 lab's floor by using a set of curved and straight PVC pipes. A cart with 4 slanted wheels can be run on the tracks by pulling a cord tied to it. The ADIS 16448 sensor was also set up at the top of the cart with the accelerometer, gyroscope and magnetometer taking measurements while moving the cart from the rail's start position up to the end of the rail.

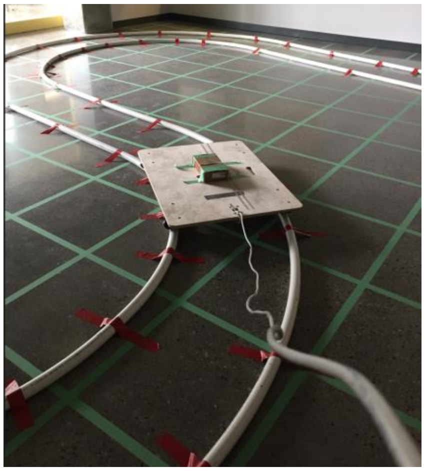

Figure 19. Rail track and cart with sensor on top. The cart can be pulled by the cord

The resulting magnetic field map along with the railing track are shown in

Figure 20.a. In

Figure 20.b the magnetic field map is created by using harmonic polynomial interpolation every 7.5 cm

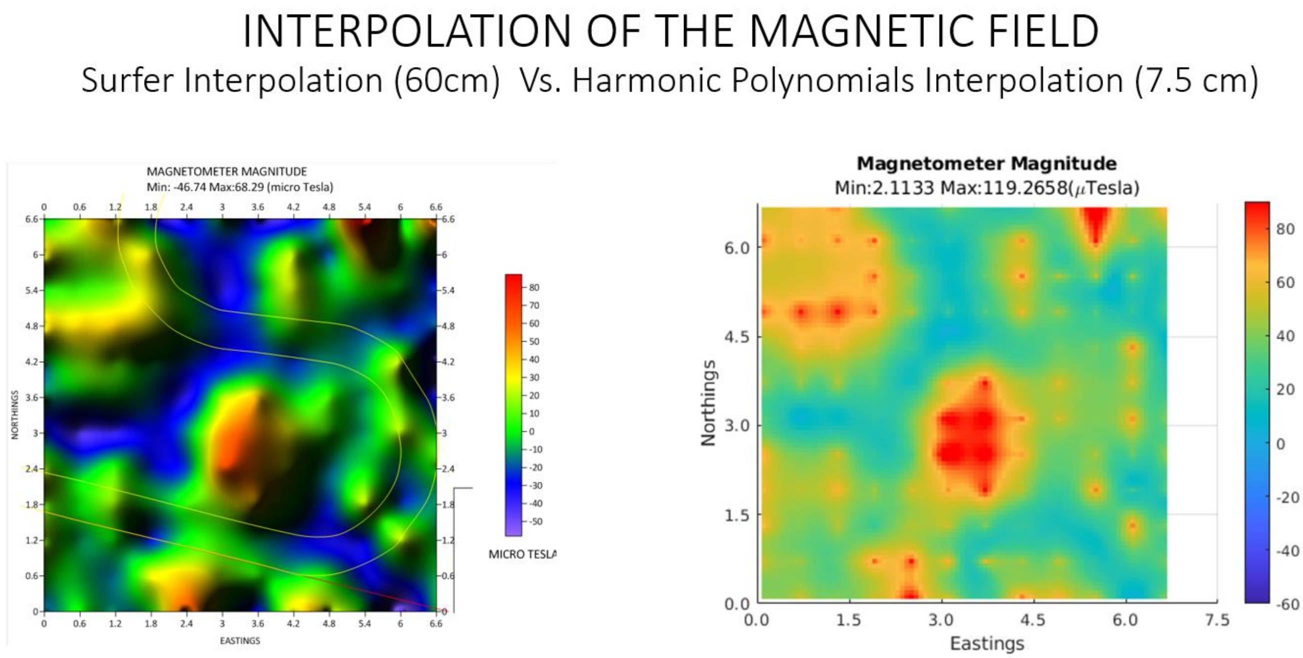

Figure 20. a) U of C G12 lab's magnetic map along with railing track. 21.b) (right) shows the use of harmonic polynomials to interpolate the field every 7.5 cm

The grid point located at the SW corner of the grid was selected as the origin of an arbitrary coordinate system. This point was assigned the coordinates of 0 meters north and 0 meters east. The grid on the floor was also used to measure the coordinates of several rail track points that were later used to reconstruct the rail track's centerline path. This centerline is used as the true trajectory. The azimuth of the centerline was calculated every 10 cm starting from the South-West end point for the entire centerline. This is depicted in

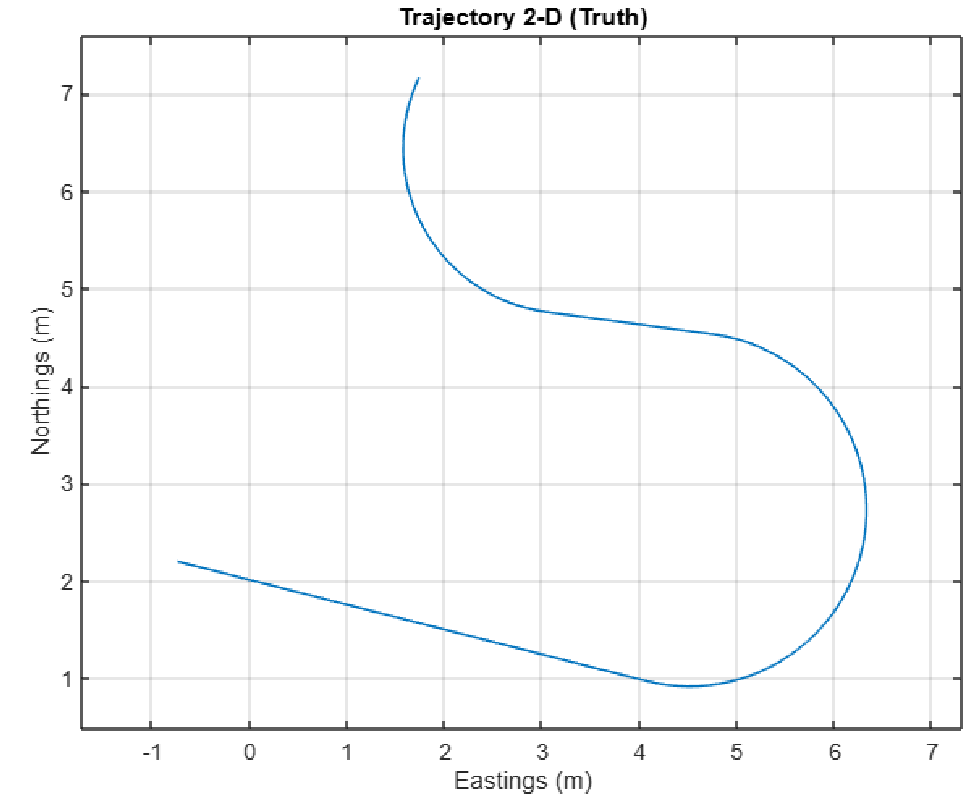
Trajectory 2-D (Truth)
Northings (m)
Eastings (m)
7
6
5
4
3
2
1
-1
0
1
2
3
4
5
6
7

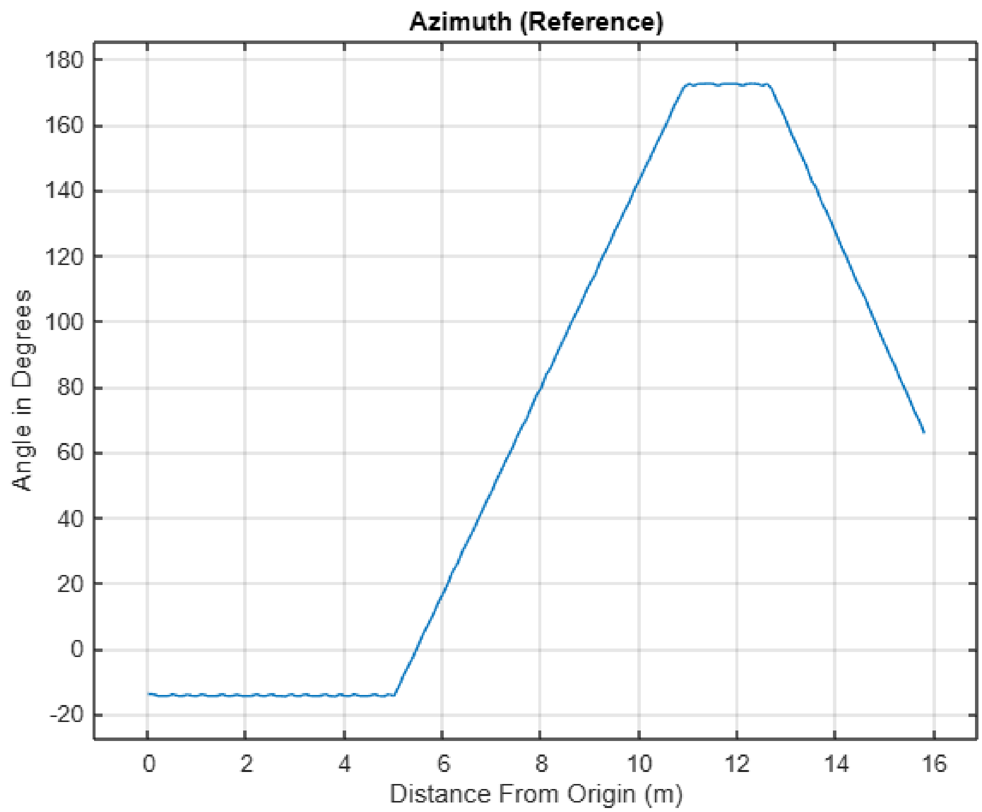
Azimuth (Reference)
Angle in Degrees
Distance From Origin (m)
180
160
140
120
100
80
60
40
20
0
-20
0
2
4
6
8
10
12
14
16

Figure 21.

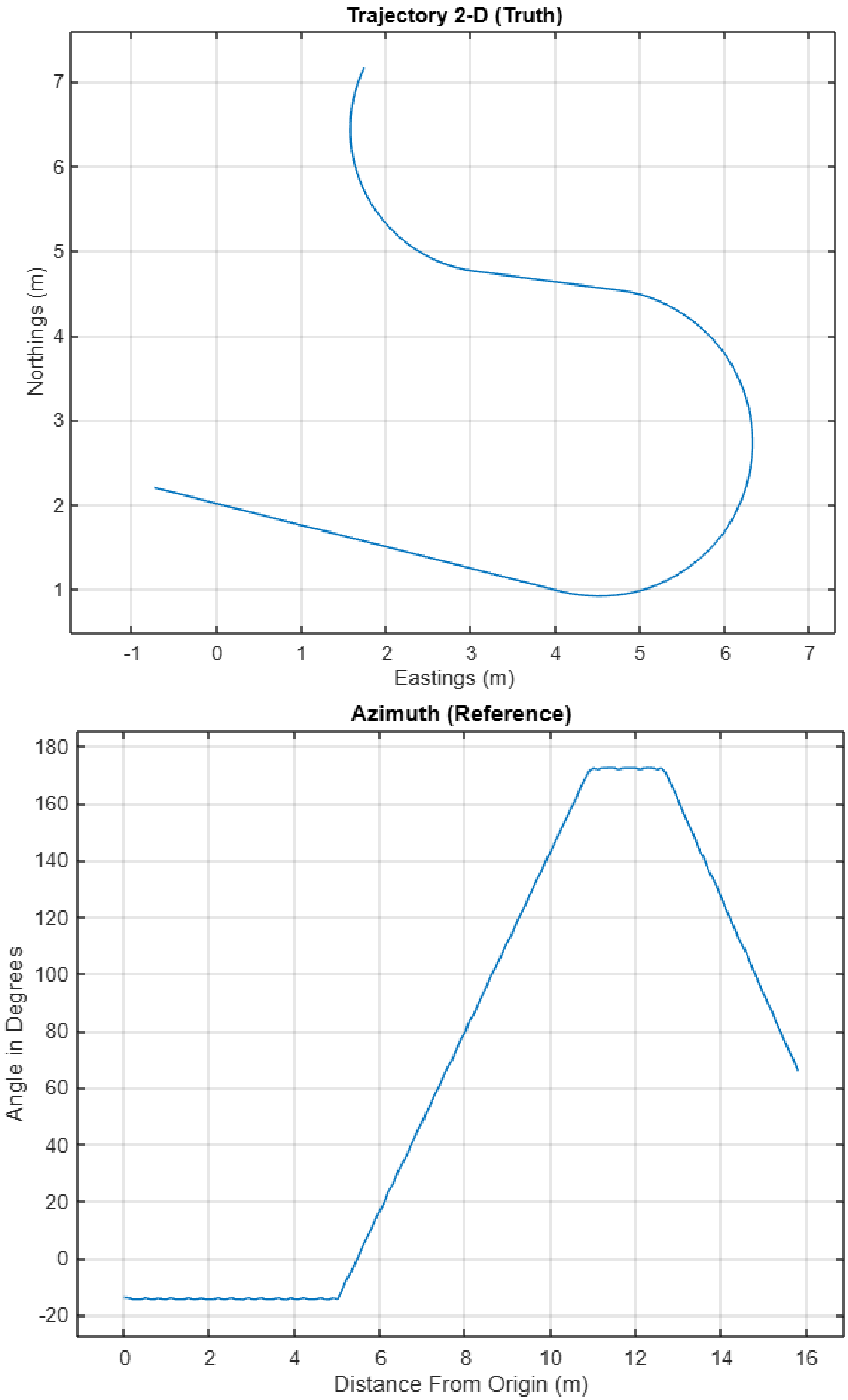

Figure 21. Plot of the rail track's centerline (above). Plot of the track's true centerline heading (below)

5.2 Test results for sensor at 3 static positions (1.2 m long)

The experiment was performed by taking magnetic field measurements for a short period of time at 3 different grid points (each separated by 60 cm). These points correspond to Grid point A, B and C and are shown in Figure 22. Harmonic polynomial parameters were estimated from the measurements taken at A and C.

Magnetic field measurements were then taken at point B, with the sensor rotated and static at different known angles. Figure 23 shows how a protractor was used to orient the sensor with respect to the grid at approximately 22°, 123°, 224°, 325° and 346°.

Harmonic polynomials were then used to estimate the magnetic field at grid point B. The estimated field at grid point B is then compared to the measurements taken by the sensor at that location. If the readings match those of the estimated field, then the sensor must have the same orientation. Otherwise, the sensor has a different orientation, which can be obtained by the angle formed between the two magnitude vectors projected into the horizontal plane.

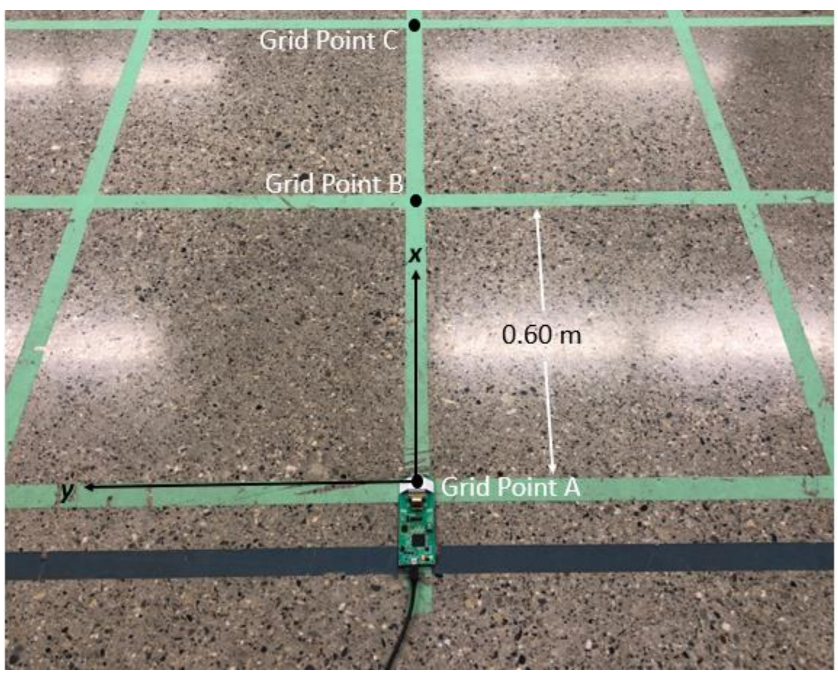

Figure 22. Magnetic field measurements taken at grid points A, B and C. The grid spacing is 0.60 m. The sensor's ***x*** *axis is aligned to the three points. Sensor's measurements at A and C have the same orientation, but at point B, measurements were made with 5 different orientations*

Figure 23. Magnetic field measurements taken at grid point B, with different sensor orientations. The sensor was oriented at 22°, 123°, 224°, 325° and 346° with respect to the grid x axis.

The measurements are shown in Table 6, and sensor orientation estimations are shown in Table 7. Table 8 shows the heading calculations for the raw data and the error is 16.8°. Figure 24, shows a plot of magnetic magnitude vectors for the different orientations.

Table 6. Magnetic field measurements taken at grid points A, B and C

Grid Point Location	Orientation (degrees)	Measured Magnetic Field (μTesla)		
		B_x	B_y	B_z
A	0	-34.8489071	-4.1977714	-37.2315786
B	0	-14.5532571	3.4684714	28.1985857
B	22	-15.8015500	-2.7678214	27.8690000
B	123	1.7454786	-15.2745286	26.2933714
B	224	12.8178143	3.1466286	26.3443143
B	325	-9.3660643	10.0622429	28.7618929
B	346	-12.2556214	5.9641214	28.5272071
C	0	3.2821571	9.4470786	-6.8504000

Table 7. Estimated sensor orientation from estimated field at B with harmonic polynomials.

Grid Point Location	True Orientation (degrees)	Estimated Magnetic Field Using Harmonic Polynomials (From points A and C Measurements) (μTesla)			Estimated Orientation Harmonic Polynomials (degrees)	Error (degrees)
		B_x	B_y	B_z		
B	0	-6.103	2.289	-8.522	7.2	-7.2
B	22				30.5	-8.5
B	123				117.1	5.9
B	224				214.4	9.6
B	325				333.5	-8.5
B	346				354.6	-8.6

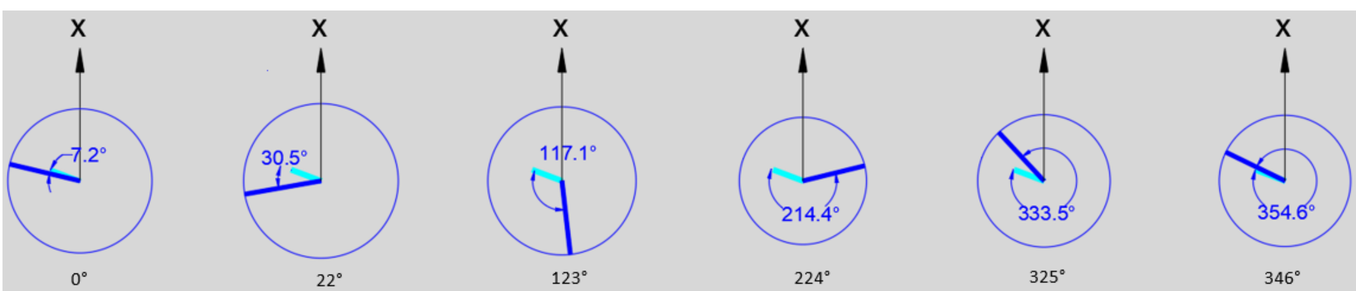

Figure 24. Magnetic vector magnitude from measurements in blue and from the estimated harmonic polynomials in cyan

Table 8. Estimated sensor orientation from raw measurements only

Grid Point Location	True Orientation (degrees)	Estimated Orientation From Raw Measurements (degrees)	Error (degrees)
B	0	0.0	0.0
B	22	23.3	-1.3
B	123	109.9	13.1
B	224	207.2	16.8
B	325	326.4	-1.4
B	346	347.5	-1.5

These results are promising as the estimated orientations from raw measurements have a maximum error of almost 17° but the estimated orientations produced by the harmonic polynomials, have an error of less than 10°.

To be able to get a more accurate solution, the estimation of the parameters for a fourth-degree harmonic polynomials, require at least 8 points with magnetic field measurements, and these points should enclose the point of interest in 3D-space. It is possible to obtain a solution with only one point, but it becomes less accurate as the distance from the known point increases.

5.3 Test results for sensor at 11 static positions (along 0.6 m)

Considering that the space in between points A and C is about 1.2 meters and looking to improve the accuracy of the estimated orientation, it was decided to test the accuracy of the harmonic polynomials for a shorter distance by using grid points A and B instead.

With the sensor having the same orientation with respect to the floor grid, magnetic field measurements were taken every 5 cm between points A and B, meaning that 11 points were measured and are depicted in Figure 25 below. Harmonic polynomials were constructed by taking the measured field from points A and B only and they were used to estimate the field at each of the 11 points.

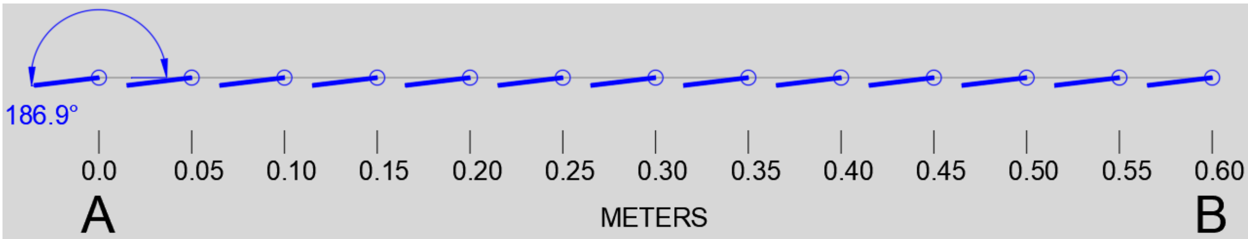

Figure 25. The 60cm space divided every 5 cm. The blue lines represent the magnetic magnitude vectors in a constant magnetic field, where the azimuth of a line measured at any point on the line must be constant.

Magnetic field measurements were compared to the estimated field values, and this is shown in Figure 26, Figure 27 and Figure 28. The measurements show more resolution while the estimated field is very smooth.

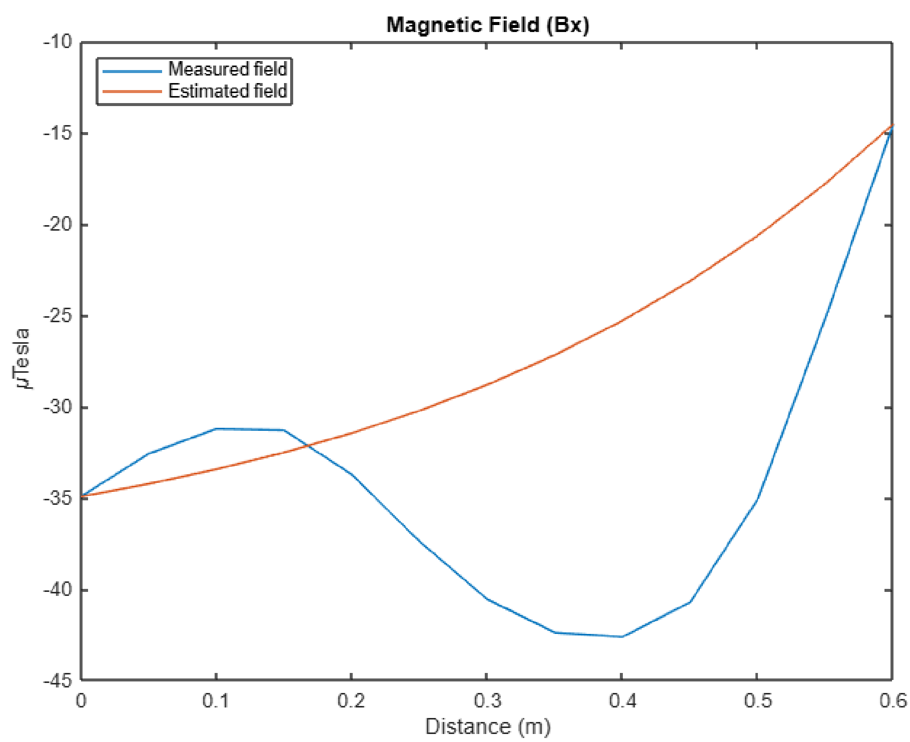

Figure 26. Plot of magnetometer X axis measurements every 5cm (blue line) and estimated field with harmonic polynomials (in red).

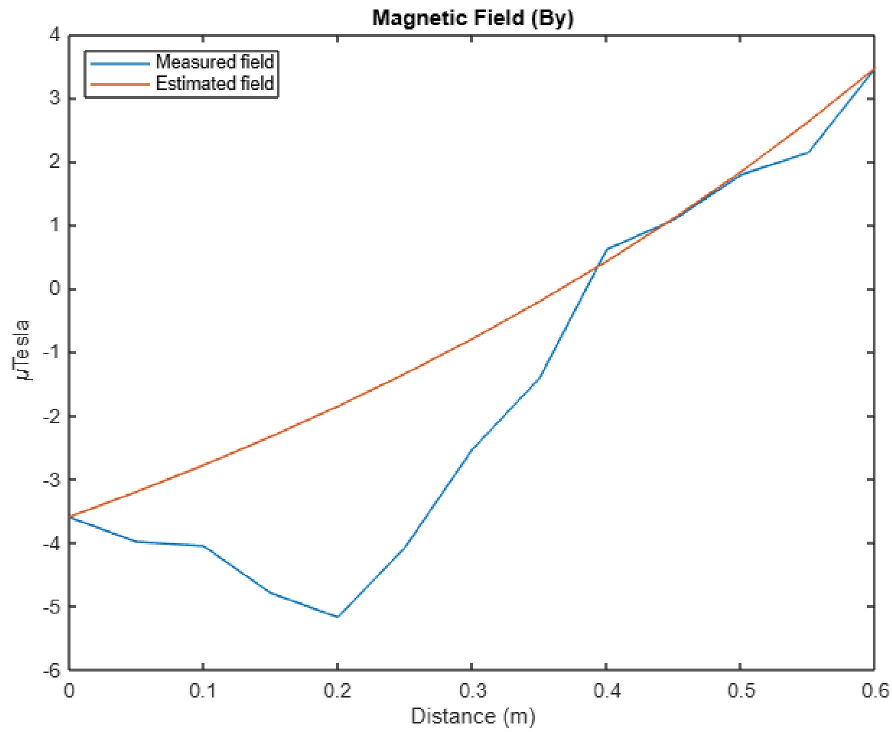

Figure 27. Plot of magnetometer Y axis measurements every 5cm (blue line) and estimated field with harmonic polynomials (in red).

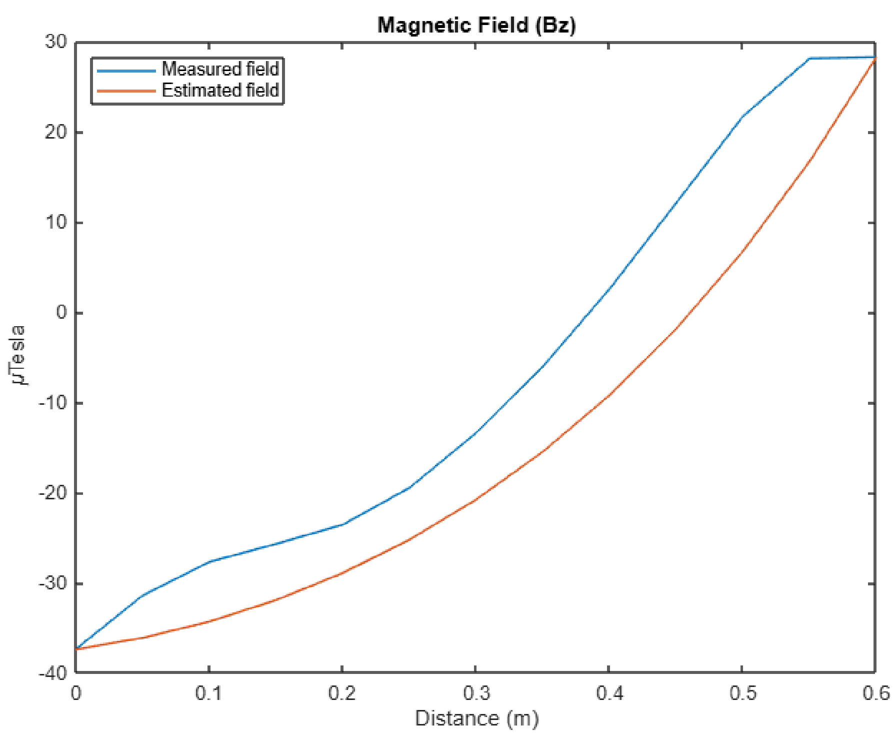

Figure 28. Plot of magnetometer Z axis measurements every 5cm (blue line) and estimated field with harmonic polynomials (in red).

With respect to the sensor orientation, all the 11 sensor positions were approximately aligned with the grid line, The grid line has an approximate heading of 186.9° from A to B or, 6.9° from B to A. This means that at each position the measured magnetic heading should be at or close to 6.9°. This assuming a constant geomagnetic field, where the heading of the line must be always the same at any point on the line. This was illustrated with blue lines in Figure 25 above.

Table 9 shows that for the raw measurements, the error varies and has a maximum error of about 20°. This error is most likely caused by the magnetic anomalies close to this location. This can be better appreciated in Figure 29 below.

Table 9. Sensor orientations obtained from magnetometer measurements between grid points A and B, every 5cm.

Grid Point Location	Distance From A (m)	B to A Magnetic Azimuth (degrees)	Measured Magnetic Field (μT)			Measured Magnetic Azimuth (degrees)	Error (degrees)
			$\boldsymbol{B_x}$	$\boldsymbol{B_y}$	$\boldsymbol{B_z}$		
A	0.00	6.9	-34.85	-4.20	-37.23	6.9	0.0
	0.05	6.9	-32.60	-3.98	-31.48	7.0	0.1
	0.10	6.9	-31.24	-4.05	-27.74	7.4	0.5
	0.15	6.9	-31.32	-4.79	-25.74	8.7	1.8
	0.20	6.9	-33.74	-5.17	-23.62	8.7	1.8
	0.25	6.9	-37.40	-4.07	-19.53	6.2	-0.7
	0.30	6.9	-40.56	-2.53	-13.45	3.6	-3.3
	0.35	6.9	-42.40	-1.41	-6.10	1.9	-5.0
	0.40	6.9	-42.63	0.61	2.51	-0.8	-7.7
	0.45	6.9	-40.74	1.08	12.05	-1.5	-8.4
	0.50	6.9	-35.08	1.79	21.64	-2.9	-9.8
	0.55	6.9	-25.15	2.13	28.05	-4.9	-11.7
B	0.60	6.9	-14.55	3.47	28.20	-13.4	-20.3

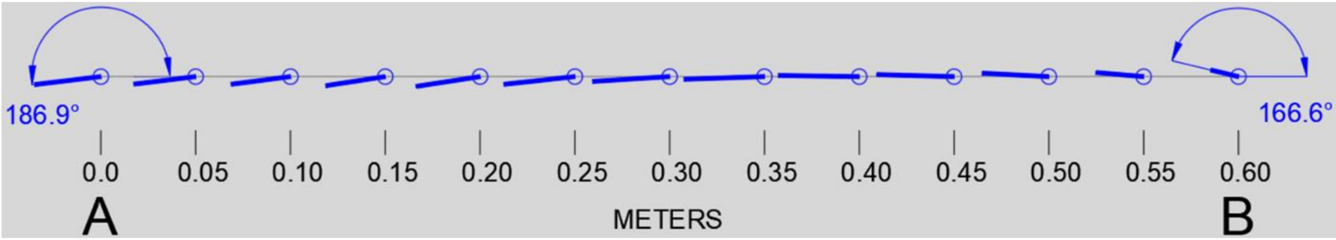

Figure 29. Due to magnetic anomalies, the measured magnetic vector magnitude changes its direction at each position, and generates a 20° azimuth error at point B.

When the magnetic field is modelled with harmonic polynomials, the estimated magnetic azimuth is subtracted from the raw magnetic azimuth to find the sensor's relative change in heading. The maximum error per each station shown in *Table* 10 is under 7°. The ideal situation would be to have this relative change in orientation closer to 0°. The results are illustrated in Figure 30.

Table 10.Estimated sensor orientation based on modelled magnetic field between grid points A and B, every 5cm.

Grid Point Location	Distance From A (m)	B to A Magnetic Azimuth (degrees)	Estimated Magnetic Field Harmonic Polynomials (Based on points A and B) (µTesla)			Estimated Magnetic Azimuth (degrees)	Change In Orientation (Measured – Estimated) (degrees)
			B_x	B_y	B_z		
A	0.00	6.9	-34.95	-3.60	-37.41	5.9	1.0
	0.05	6.9	-33.96	-3.17	-36.25	5.3	1.6
	0.10	6.9	-32.36	-2.66	-34.55	4.7	2.7
	0.15	6.9	-30.29	-2.07	-31.69	3.9	4.8
	0.20	6.9	-27.92	-1.44	-26.43	2.9	5.8
	0.25	6.9	-25.45	-0.76	-17.21	1.7	4.5
	0.30	6.9	-23.03	-0.06	-4.29	0.2	3.4
	0.35	6.9	-20.83	0.63	8.55	-1.7	3.6
	0.40	6.9	-18.93	1.31	17.59	-4.0	3.1
	0.45	6.9	-17.38	1.95	22.69	-6.4	4.9
	0.50	6.9	-16.18	2.53	25.42	-8.9	6
	0.55	6.9	-15.27	3.04	27.06	-11.3	6.4
B	0.60	6.9	-14.55	3.47	28.20	-13.4	0.0

The procedure above assumed the magnetic field is known at positions A and B and harmonic polynomials were calculated from those two points. The points in between were estimated with these harmonic polynomials.

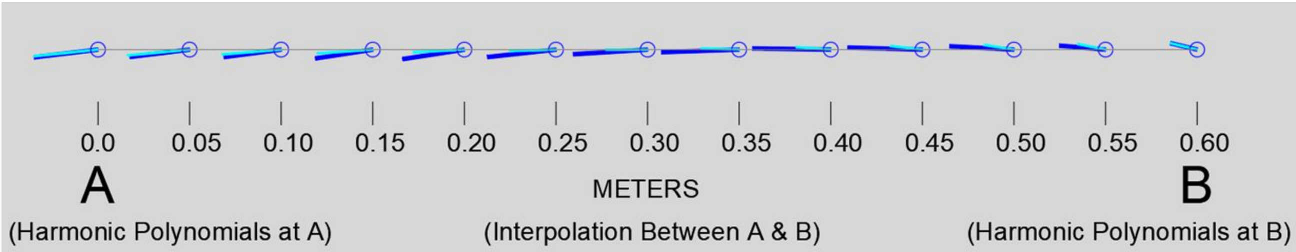

Figure 30. Estimation of the magnetic field magnitude vector from Harmonic Polynomials at each station (in cyan)

Another possibility is to calculate harmonic polynomials with only one initial point and then recalculating them with measurements obtained when the sensor is located at other stations. This can be particularly useful when the sensor is moving. I am calling this method "incremental harmonic polynomials" To start harmonic polynomials were calculated only from point A, then the magnitude vector of the magnetic field is estimated for station 0.05m, also magnetometer measurements are taken when the sensor is located at this station and estimated and measured magnitude vectors' orientation can be compared to detect if the sensor has changed its orientation or not. The measurements at station 0.05m are used to recalculate harmonic polynomials and then to estimate the field at station 0.10m. This procedure is repeated for the next stations until reaching to Point B. This procedure is illustrated in Figure 31.

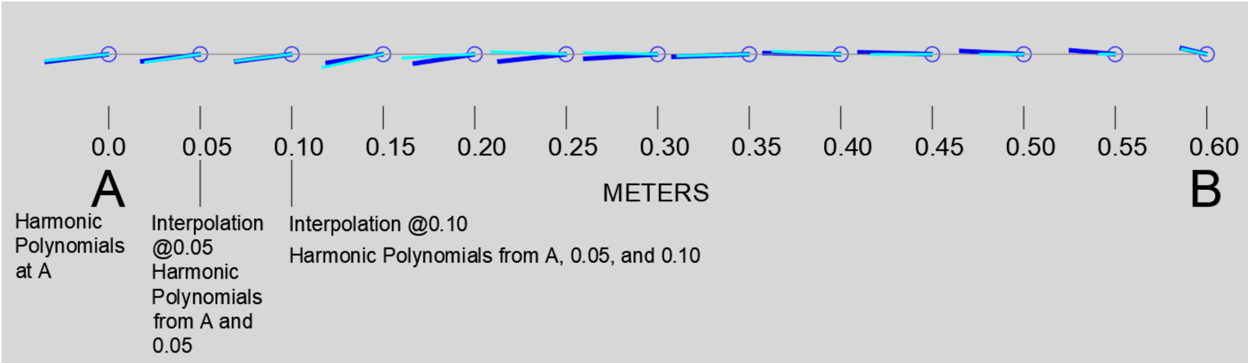

Figure 31. Incremental Harmonic Polynomials method with its estimated magnetic vector magnitude (Cyan Color)

The magnetic field modelling has improved when the incremental harmonic polynomials method is applied. The estimated field is closer to the actual measurements, and this can be seen in

Figure 32,

Figure 33 and

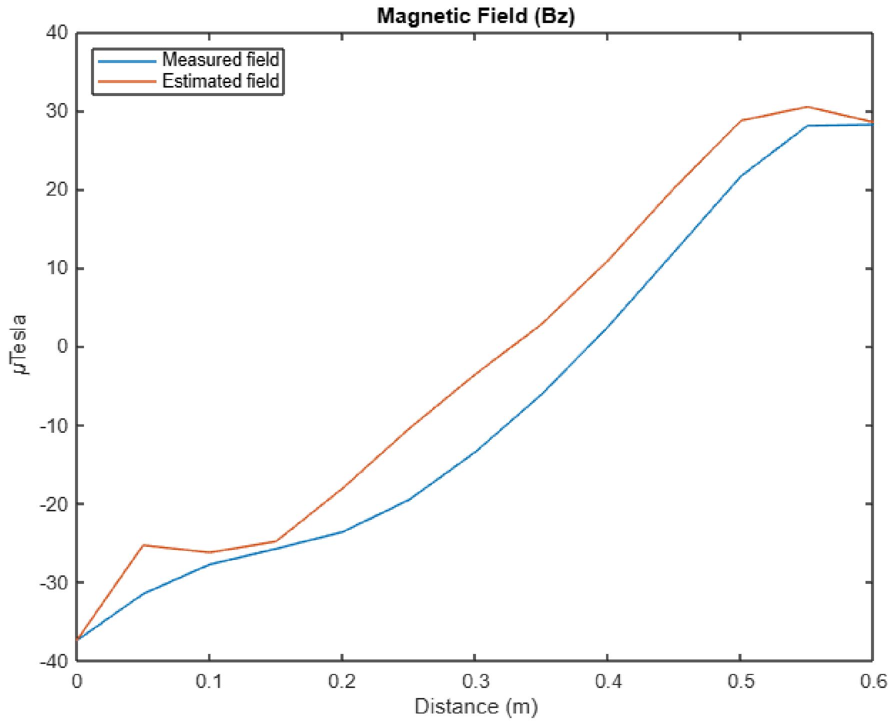

Figure 34.

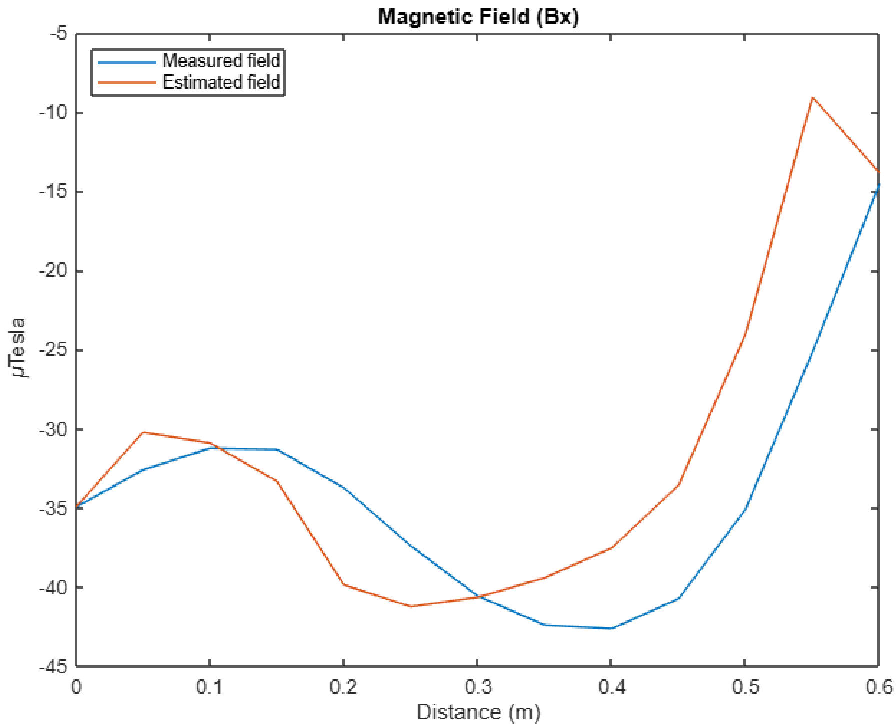

Figure 32. Plot of magnetometer X axis measurements every 5cm (blue line) and estimated field with incremental harmonic polynomials (in red).

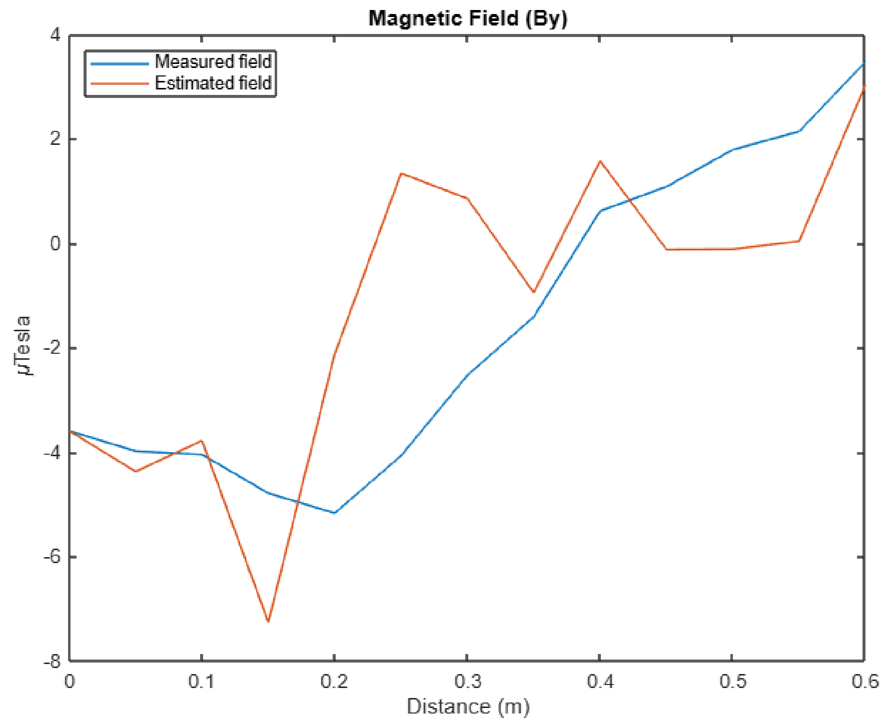

Figure 33. Plot of magnetometer Y axis measurements every 5cm (blue line) and estimated field with incremental harmonic polynomials (in red).

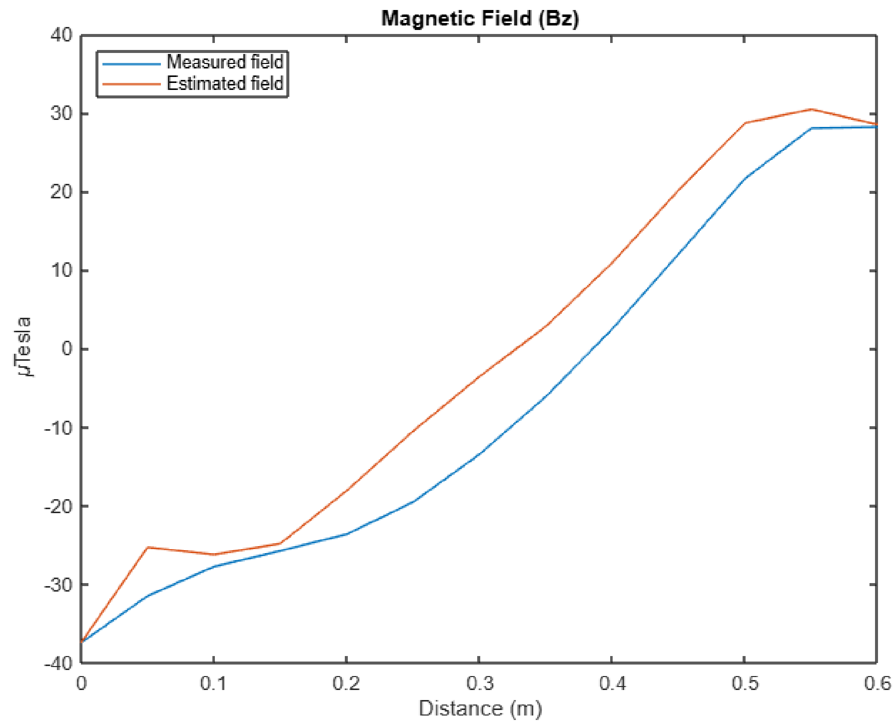

Figure 34. Plot of magnetometer Z axis measurements every 5cm (blue line) and estimated field with incremental harmonic polynomials (in red).

5.4 Test results for moving sensor on a railing track.

The dynamics for the moving sensor test, require the Mechanization Equations which were programmed in MATLAB.

The starting point of the sensor was set with approximate latitude and longitude coordinates and with an initial sensor orientation which was obtained from the raw alignment method. The latitude and longitude coordinates are important as an approximate gravity value can be obtained, and this will be used to remove the gravity vector from the accelerometer. The sensor was positioned on the approximate center of mass of the cart. The forward direction of movement was aligned with the sensor's positive x axis.

Collected data from the sensor's accelerometers and gyroscopes was corrected by bias and scale factors then fed into the extended Kalman filter algorithm to obtain an initial trajectory, heading, and velocities. These results are shown in Figure 35, Figure 36 and Figure 37.

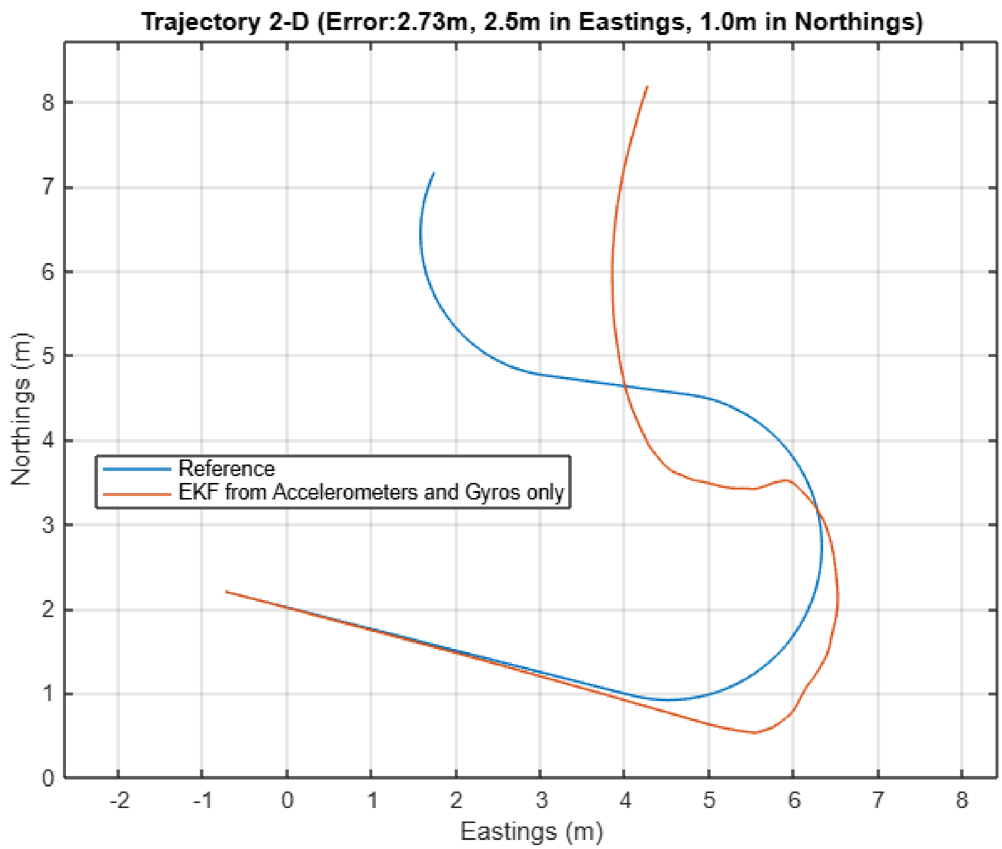

Figure 35. Reference trajectory in blue and trajectory from extended Kalman filter fed by accelerometers and gyroscope data in red. The error at the end point is about 2.7 m.

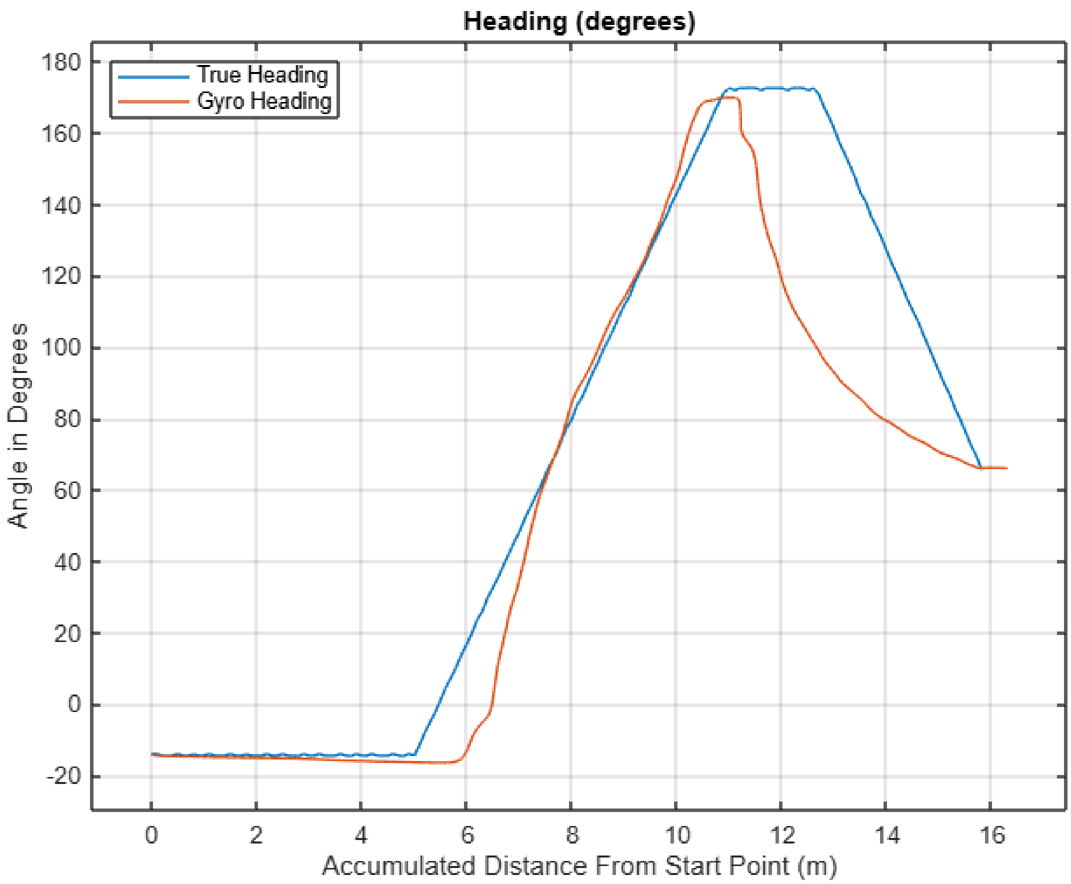

Figure 36. Heading obtained from extended Kalman filter (accelerometers and gyroscopes only).

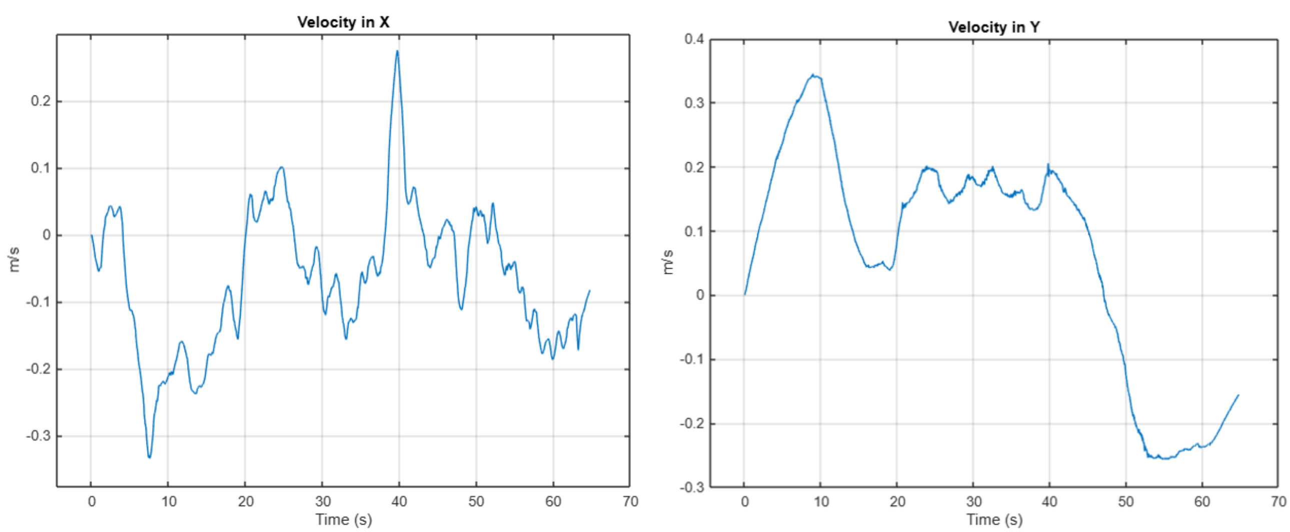

Figure 37. Velocities in X and Y axis obtained from the EKF

(accelerometers and gyroscopes only).

Magnetic measurements were corrected for hard and soft iron errors, then these measurements are mathematically leveled. The leveled magnetic field measurements are then used to calculate the harmonic polynomials at each update. An angular rate of change is calculated and then fed into the update step of the EKF. For this test, data from the gyroscopes is not used, only magnetometer data is used to estimate heading and to produce the estimated trajectory. These results are shown in *Figure 38*, *Figure 39* and *Figure 40*.

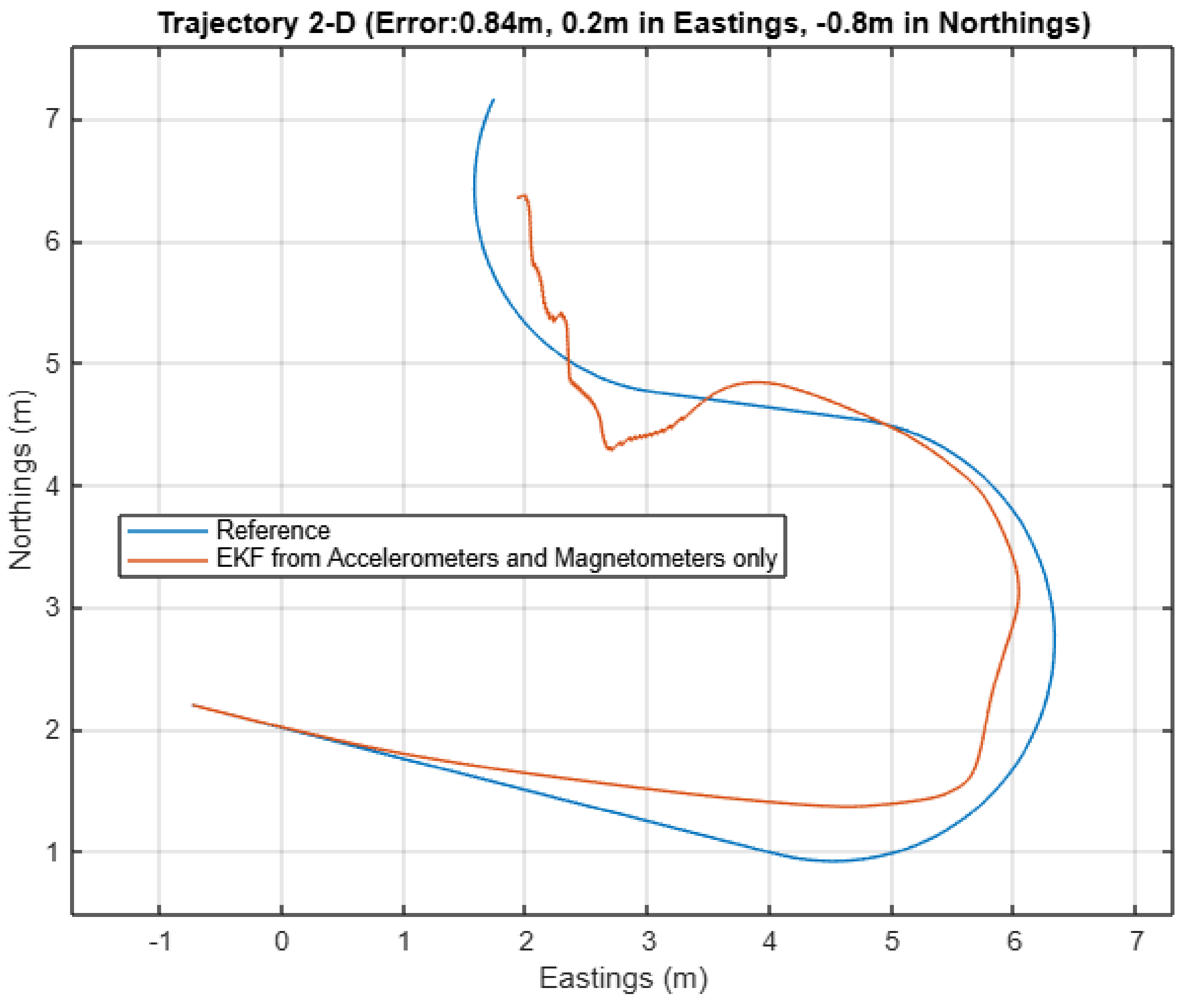

Figure 38. Reference trajectory in blue and trajectory from extended Kalman filter fed by accelerometers and magnetometer data in red. The error at the end point is about 0.84 m.

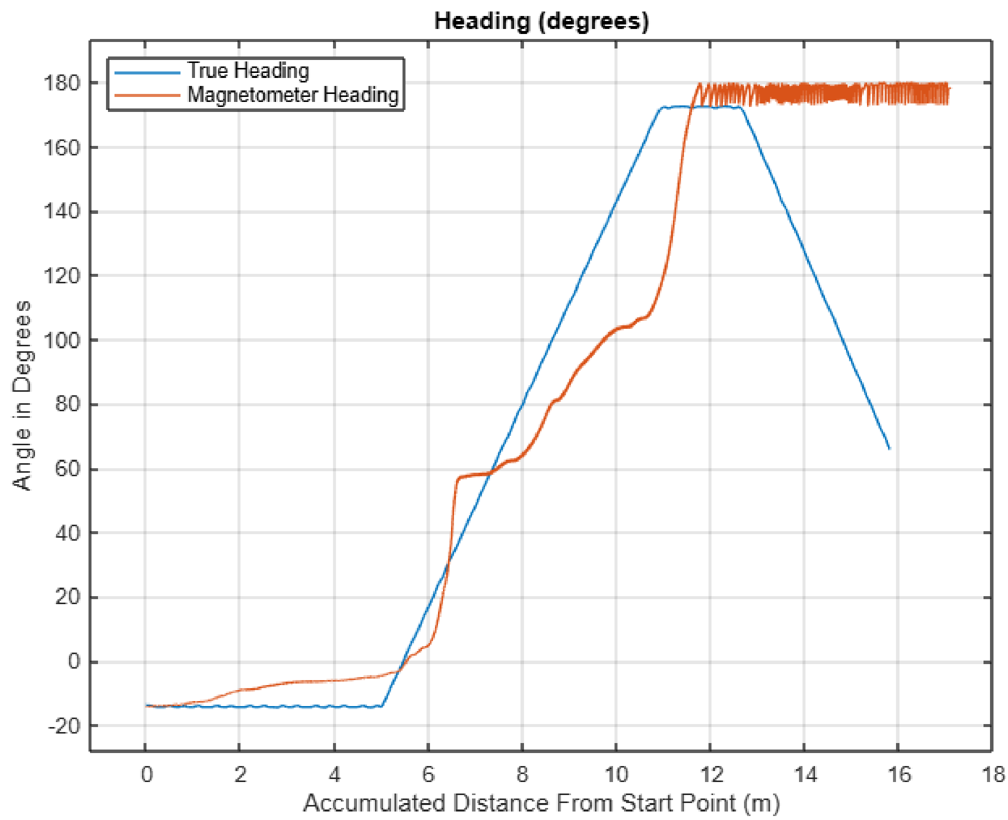

Figure 39. Reference heading in blue. Heading from extended Kalman filter in red (accelerometers and magnetometers only).

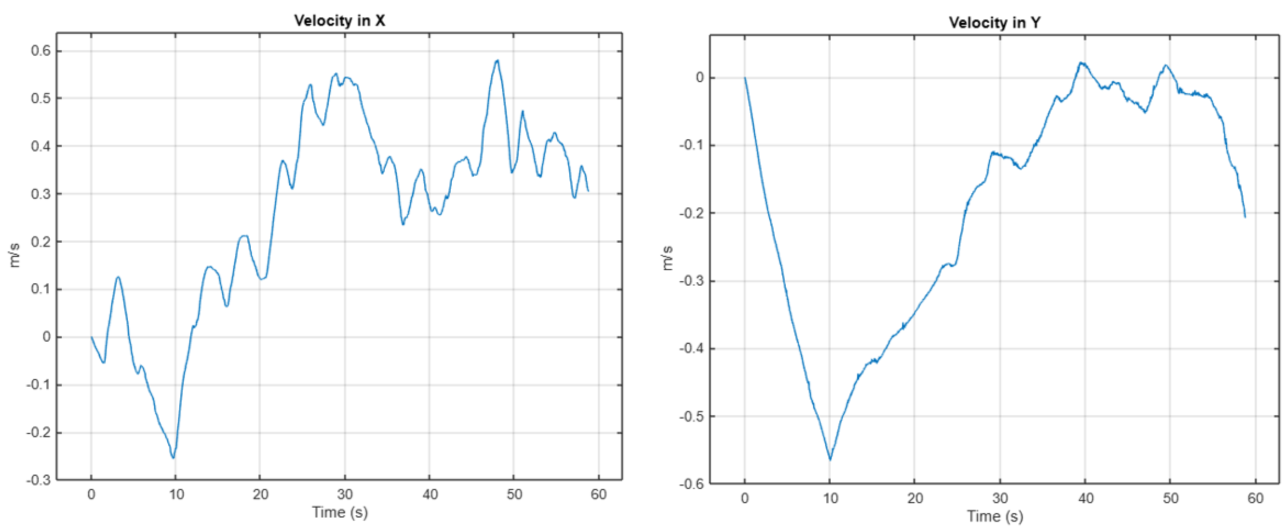

Figure 40. Velocities and the X and Y-axes obtained from the EKF

(accelerometers and magnetometers only).

For the following test, along with the magnetometer deduced heading, the velocity obtained from the magnetic field is also added. Again, data from the gyroscopes is not used this time. The results are shown in Figure 41, Figure 42, Figure 43 and Figure 44.

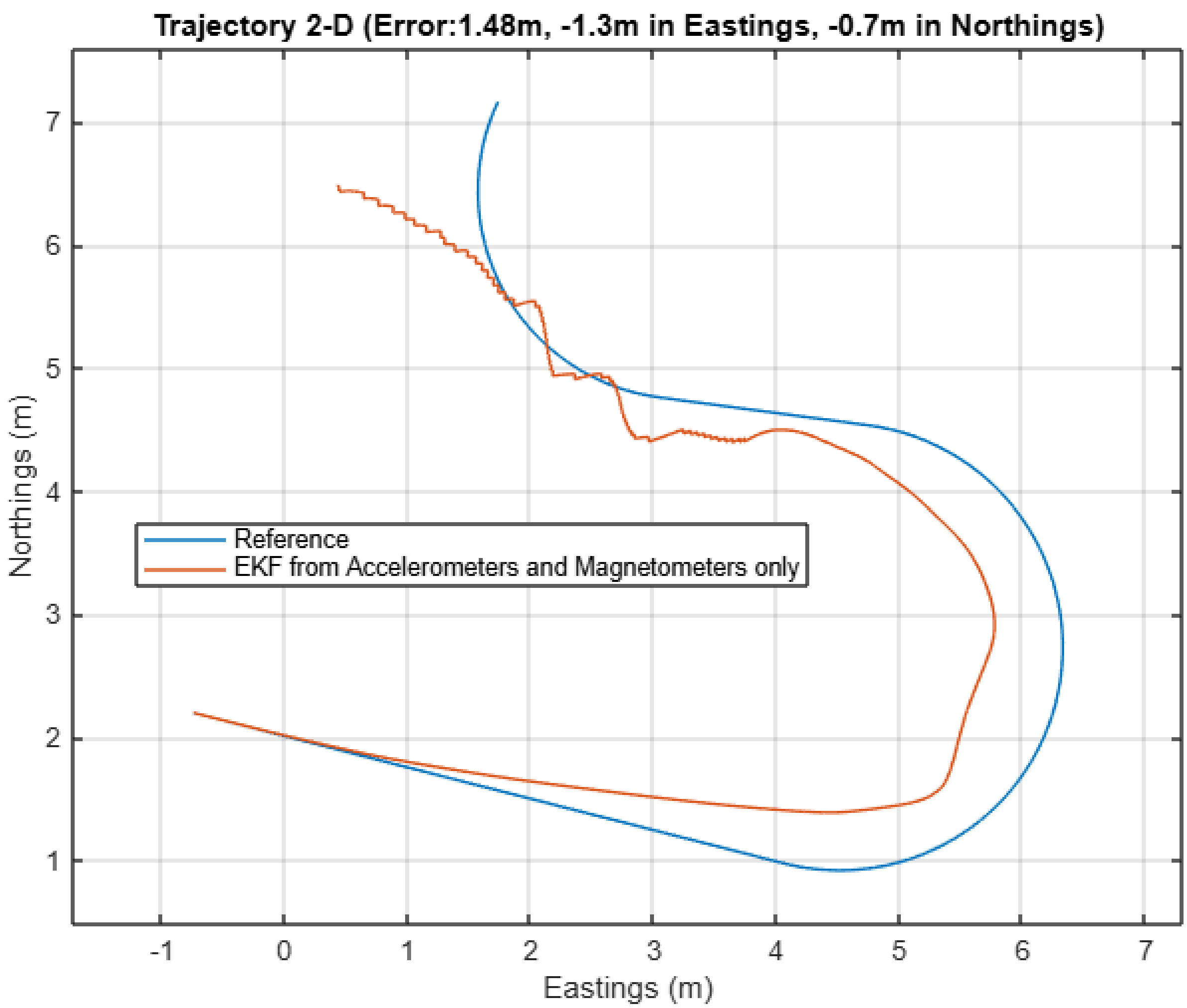

Figure 41. Reference trajectory in blue and trajectory from extended Kalman filter fed by accelerometers, heading and velocity calculated from magnetometer data in red. The error at the end point is about 1.5 m.

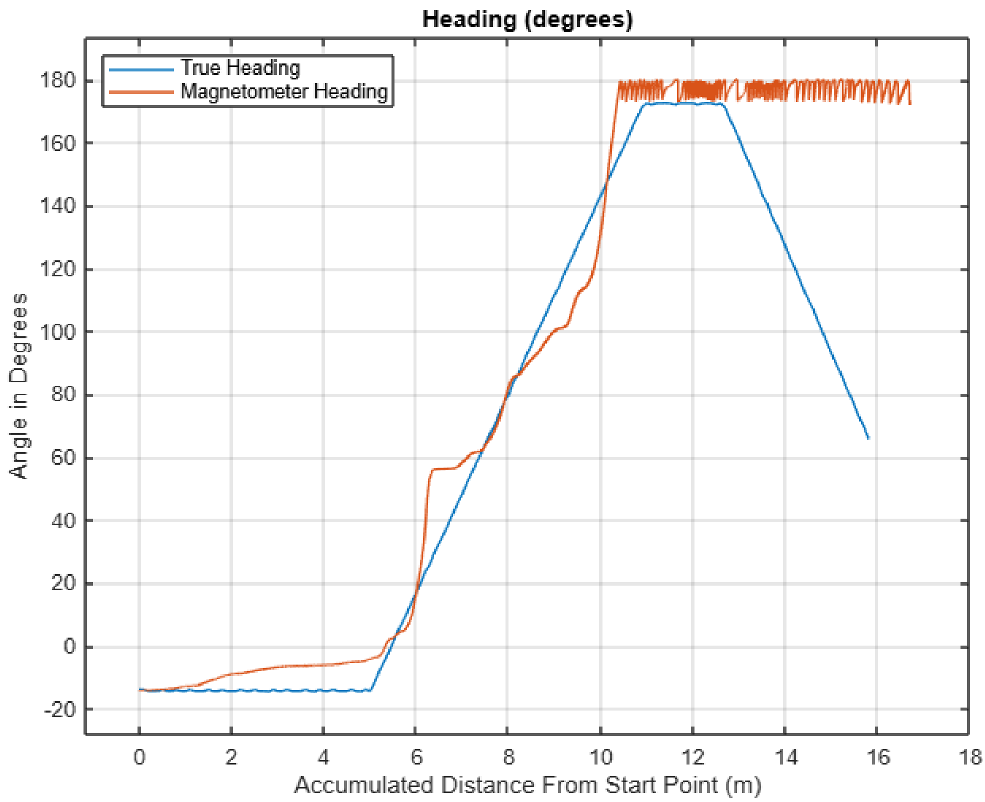

Figure 42. Reference heading in blue. Heading from extended Kalman filter (Accelerometers, Magnetometers and Magnetic Velocity)

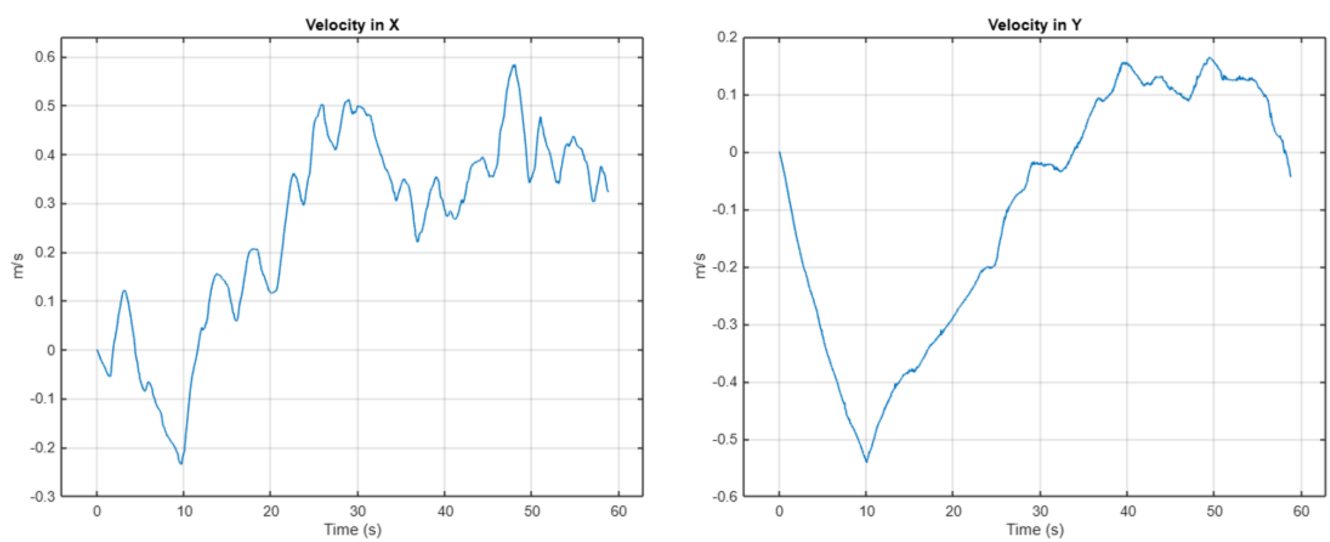

Figure 43. Total velocities obtained from the EKF (accelerometers and magnetometers only).

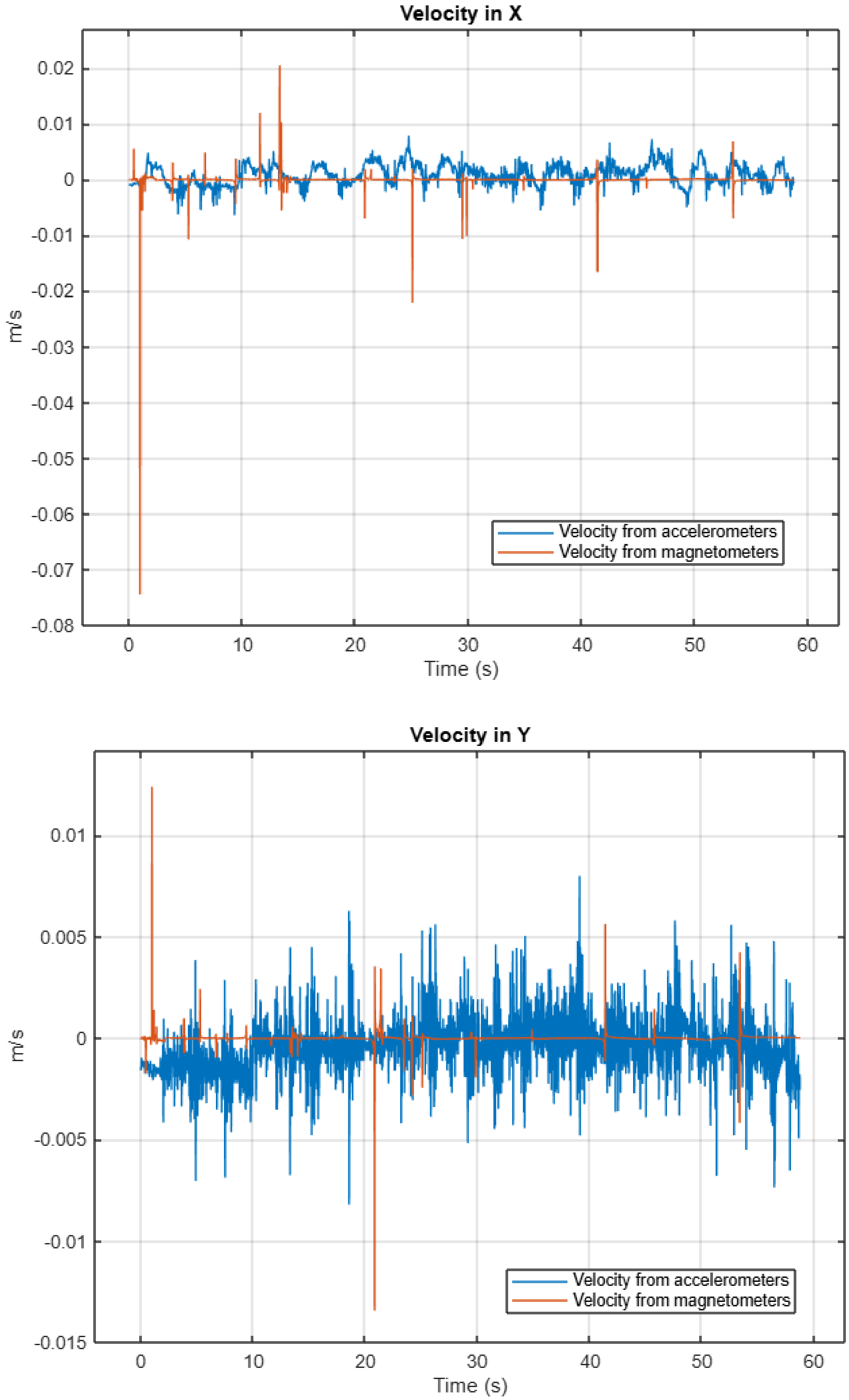

Figure 44. Magnetic velocities in X and Y axis compared to velocities from accelerometers. Magnetic velocities scaled down 10,000 times

5.5 Chapter Summary

To be able to understand the contribution of bringing magnetometer data, three different tests were performed. All of them used the extended Kalman filter. The performance will be based on the error at the end of the trajectory and by visually checking how the estimated trajectory follows the true trajectory:

- Accelerometer and Gyroscope data fusion: Figure 35 shows how the horizontal trajectory deviates a from the reference trajectory. The total error at the end is about 2.7 m, which corresponds to 2.5 m in eastings and 1.0 m in northings. Considering that the track is only 15.75 m long, these errors are high. These errors are expected as there is no other source of information to correct for accelerometer and/or gyroscopes errors. The heading for these sensor's data fusion shows that there are heading differences with respect to the true heading.
- Accelerometer and Magnetometer's heading data fusion: Figure 38 shows how the horizontal trajectory deviates a from the reference trajectory, even though this time compared to the previous test, the estimated trajectory follows more closely the true trajectory. The total error at the end is about 0.84 m, which corresponds to 0.2 m in eastings and -0.8 m in northings. This error compared to the previous test is smaller and this shows a benefit of using the magnetic heading. The heading for these sensor's data fusion also shows heading differences with respect to the true heading.
- Accelerometer, Magnetometer's heading and Magnetic velocity data fusion: Figure 41 shows how the horizontal trajectory deviates a from the reference trajectory and for this test the estimated trajectory is very similar to the previous test. The total error at the end is about 1.5 m, which corresponds to 1.3 m in eastings and -0.7 m in northings. Introducing the velocity obtained from the magnetometer makes the filter unstable at the end and this is noticed by zigzag created in the estimated trajectory. By adding magnetic velocities, the heading still has differences with respect to the true heading. Figure 44 shows a plot comparing the velocities from the accelerometer and the velocities obtained from the magnetometer. The velocities obtained from the changes in the magnetic field show big spikes. These spikes were scaled down 10,000 to be able to plot the graph. The EKF probably ignored these spikes.

Chapter 6: CONCLUSIONS AND RECOMMENDATIONS

6.1 Conclusions

Navigation inside the well bore relies on sensors and one of the fundamental tasks to improve navigational accuracy is to find the errors that affect a sensor's measurements so they can be removed or mitigated. Deterministic, short- and long-term errors were investigated for the MEMS IMU ADIS16448 sensor. The INS dead reckoning navigation mode was applied, then magnetometer measurements provided uncorrelated sensor orientation and velocity which were fused with a centralized Kalman Filter.

Given the presence of magnetic anomalies in the lab room, the results show that the use of harmonic polynomials improved the estimation of the heading, and even when comparing it to the one produced by the gyroscope, the results seem to be similar or even better than the gyroscope. It can be said that the use of harmonic polynomials for the heading estimation along with the EKF could greatly improve the navigation solution for indoor or underground navigation applications.

Harmonic polynomials rely on knowing the position of the sensor, but this is obtained from the accelerometers and these coordinates would deteriorate rapidly with time. It is then necessary to provide extra information like for example from an odometer or for the case of directional drilling the drilling rate. Combining both the gyroscope and the magnetometer measurements could improve the sensors heading estimation, but the purpose of this research was to investigate if the magnetometer data was usable at all or not.

The velocity produced by the magnetometer also requires knowing the sensor's rotation rate, but this is also obtained from the INS estimated values. Looking at the velocity graphs, there are several prominent spikes, and it seems that this corresponds to the sensor passing through the track's curves sections. The spikes might be an indication of the presence of centripetal acceleration at these locations. But these spikes are too high to be accepted as a reasonable value and the EKF seem to ignore it during innovation. This situation needs to be further investigated.

6.2 Recommendations

The recommendations for future work are the following:

1. Noise in the magnetic field can be reduced by doing upward continuation as this acts as a low-pass filter.
2. Modelling of the magnetic field might also be improved by adding other spatially distributed magnetometers.
3. Adding and odometer/drilling rate might improve the modelling of harmonic polynomials as this might also improve positional estimations (To reduce the Chicken-Egg problem).
4. For the wellbore situation, adding a pressure sensor might also help improving positional estimation.
5. The velocity obtained from the magnetic field need to be further investigated, this will require the use of an external velocity sensor to correlate the magnetic produced velocity.

References

Adis16448.pdf. (n.d.). Retrieved October 26, 2023, from https://www.analog.com/media/en/technical-documentation/data-sheets/adis16448.pdf

Aggarwal, P. (2010). *MEMS-based integrated navigation*. Artech House. https://books.google.ca/books?hl=en&lr=&id=IfLdaZ_evpgC&oi=fnd&pg=PR5&dq=Aggarwal,+P.+(2010).+MEMS-based+integrated+navigation.+Artech+House.&ots=KTO8PknDqm&sig=VUShBe_58vcdxFxHluWvLC9VkAQ

Allan, D. W. (1966). Statistics of atomic frequency standards. *Proceedings of the IEEE*, *54*(2), 221–230. https://ieeexplore.ieee.org/abstract/document/1446564/

Barbour, N. M. (2010). Inertial navigation sensors. *NATO RTO Lecture Series, RTO-EN-SET-116, Low-Cost Navigation Sensors and Integration Technology*. https://apps.dtic.mil/sti/citations/ADA581016

Chung, J., Donahoe, M., Schmandt, C., Kim, I.-J., Razavai, P., & Wiseman, M. (2011). Indoor location sensing using geo-magnetism. *Proceedings of the 9th International Conference on Mobile Systems, Applications, and Services*, 141–154. https://doi.org/10.1145/1999995.2000010

DOE Explains...Stellarators. (n.d.). Energy.Gov. Retrieved October 24, 2023, from https://www.energy.gov/science/doe-explainsstellarators

Dorveaux, E., Boudot, T., Hillion, M., & Petit, N. (2011). Combining inertial measurements and distributed magnetometry for motion estimation. *Proceedings of the 2011 American Control Conference*, 4249–4256. https://ieeexplore.ieee.org/abstract/document/5990993/

El-Diasty, M., & Pagiatakis, S. (2010). Calibration and stochastic modelling of i nertial navigation sensor errors. *Positioning (POS) Journal Information*, 80. https://file.scirp.org/pdf/POS_08_01_2010070610391660.pdf#page=83

Estes, R. A., & Epplin, D. M. (2000). Development of a robust gyroscopic orientation tool for MWD operations. *SPE Annual Technical Conference and Exhibition?*, SPE-63274. https://onepetro.org/SPEATCE/proceedings-abstract/00ATCE/All-00ATCE/132252

Gelb, A. (1974). *Applied optimal estimation*. MIT press. https://books.google.ca/books?hl=en&lr=&id=KlFrn8lpPP0C&oi=fnd&pg=PA1&dq=Gelb,+A.+(1974).+Applied+optimal+estimation,+1974.+Applied+Optimal+Estimation.&ots=dCVP2n8xtJ&sig=2IOn18rOaZL7rjUmbC1nRFHNwII

Jamieson, A., McGregor, A., Stigant, J., Weston, J., Grindrod, S., & McRobbie, D. (2012). Introduction to wellbore positioning. *ISCWSA Inititative for Published through Research Office of University of HighLands and Islands*.

Joshi, S. D., & Ding, W. (1991). The cost benefits of horizontal drilling. *Proc. American Gas Association*, 29–1.

Kabirzadeh, H., Rangelova, E., Lee, G. H., Jeong, J., Woo, I., Zhang, Y., & Kim, J. W. (2018). Dynamic error analysis of measurement while drilling using variable geomagnetic in-field referencing. *SPE Journal*, *23*(06), 2327–2338. https://onepetro.org/SJ/article-abstract/23/06/2327/206781

Kok, M., Wahlström, N., Schön, T. B., & Gustafsson, F. (2013). MEMS-based inertial navigation based on a magnetic field map. *2013 IEEE International Conference on Acoustics, Speech and Signal Processing*, 6466–6470. https://ieeexplore.ieee.org/abstract/document/6638911/

Maxwell, J. C. (1996). *A dynamical theory of the electromagnetic field*. Wipf and Stock Publishers. https://books.google.ca/books?hl=en&lr=&id=p1pKAwAAQBAJ&oi=fnd&pg=PR12&dq=Maxwell,+J.+C.+(1996).+A+dynamical+theory+of+the+electromagnetic+field.+Wipf+and+Stock+Publishers&ots=w0rj8m69mD&sig=qIhkkcUqI8qWEcuCNroPeJFb6g4

Miles, E. P., & Williams, E. (1955). A basic set of homogeneous harmonic polynomials in k variables. *Proceedings of the American Mathematical Society*, *6*(2), 191–194. https://www.jstor.org/stable/2032337

Noureldin, A., Karamat, T. B., & Georgy, J. (2012). *Fundamentals of inertial navigation, satellite-based positioning and their integration*. Springer Science & Business Media. https://books.google.ca/books?hl=en&lr=&id=a-BqvoCd2RkC&oi=fnd&pg=PR7&dq=Noureldin,+A.,+Karamat,+T.+B.,+%26+Georgy,+J.+(2012).+Fundamentals+of+inertial+navigation,+satellite-based+positioning+and+their+integration&ots=9KK1yK3PaP&sig=6DjKyi0etsRoT_XWT6O3SpSLvVU

Noureldin, A. M. (2002). *New measurement-while-drilling surveying technique utilizing sets of fiber optic rotation sensors*. Citeseer. https://citeseerx.ist.psu.edu/document?repid=rep1&type=pdf&doi=4730cf80567959910f6ec884e1dac7fbfbfd64c4

Probert, P. (2011). High-performance interpolation of stellarator magnetic fields. *IEEE Transactions on Plasma Science*, *39*(4), 1051–1054. https://ieeexplore.ieee.org/abstract/document/5716685/

Ripka, P. (2001). *Magnetic sensors and magnetometers*. Artech house. https://repository.vnu.edu.vn/handle/VNU_123/92894

Rodrigo Ramon, J. L. (2018). *Maxwellian Interpolation of Magnetic fields on a grid* [PhD Thesis]. https://fse.studenttheses.ub.rug.nl/id/eprint/17945

Shelkholeslami, B. A., Schlottman, B. W., Seidel, F. A., & Button, D. M. (1991). Drilling and production aspects of horizontal wells in the Austin Chalk. *Journal of Petroleum Technology*, *43*(07), 773–779. https://onepetro.org/JPT/article-abstract/43/07/773/53522

Thorogood, J. L., & Knott, D. R. (1990). Surveying techniques with a solid-state magnetic multishot device. *SPE Drilling Engineering*, *5*(03), 209–214. https://onepetro.org/DC/article-abstract/5/03/209/168455

Torkildsen, T., Edvardsen, I., Fjogstad, A., Saasen, A., Amundsen, P. A., & Omland, T. H. (2004). Drilling fluid affects MWD magnetic azimuth and wellbore position. *IADC/SPE Drilling Conference*. https://onepetro.org/SPEDC/proceedings/04DC/SPE-87169-MS/70748

Vissière, D., Martin, A., & Petit, N. (2007). Using distributed magnetometers to increase IMU-based velocity estimation into perturbed area. *2007 46th IEEE Conference on Decision and Control*, 4924–4931. https://ieeexplore.ieee.org/abstract/document/4434809/

Vissiere, D., Martin, A., & Petit, N. (2007). Using magnetic disturbances to improve IMU-based position estimation. *2007 European Control Conference (ECC)*, 2853–2858. https://ieeexplore.ieee.org/abstract/document/7069004/

Wahlström, N., Kok, M., Schön, T. B., & Gustafsson, F. (2013). Modeling magnetic fields using Gaussian processes. *2013 IEEE International Conference on Acoustics, Speech and Signal Processing*, 3522–3526. https://ieeexplore.ieee.org/abstract/document/6638313/

Wall, J. H., & Bevly, D. M. (2005). Characterization of various IMU error sources and the effect on navigation performance. *Proceedings of the 18th International Technical Meeting of the Satellite Division of the Institute of Navigation (ION GNSS 2005)*, 967–978. https://www.ion.org/publications/abstract.cfm?articleID=6292

Wall, J. H., & Bevly, D. M. (2006). Characterization of inertial sensor measurements for navigation performance analysis. *Proceedings of the 19th International Technical Meeting of the Satellite Division of The Institute of Navigation (ION GNSS 2006)*, 2678–2685. https://www.ion.org/publications/abstract.cfm?articleID=6774

Wu, H., Pei, X., Li, J., Gao, H., & Bai, Y. (2020). An improved magnetometer calibration and compensation method based on Levenberg–Marquardt algorithm for multi-rotor unmanned aerial vehicle. *Measurement and Control*, *53*(3–4), 276–286. https://doi.org/10.1177/0020294019890627

Appendix A Normal Gravity

To obtain an approximate gravity value, the formula for the normal gravity can be used. In this formula gravity is a function of the latitude and elevation above sea level:

$$g = a_1(1 + a_2 sin^2\varphi + a_3 sin^4\varphi) + (a_4 + a_5 sin^2\varphi)h + a_6 h^2 \qquad \text{(A-1)}$$

where φ is the Latitude and h is the elevation. The coefficients a_n are defined as:

$$a_1 = 9.7803267715$$

$$a_2 = 0.0052790414$$

$$a_3 = 0.0000232718$$

$$a_4 = -0.000003087691089$$

$$a_5 = 0.000000004397731$$

$$a_6 = 0.000000000000721$$

Appendix B Stochastic Process Modelling

B.1 White Noise

White noise is a process that has a constant power density in the frequency domain. This means that power is distributed uniformly on all frequencies for an infinite range. The autocorrelation function is given by (Gelb, 1974):

$$\varphi_{nn}(\tau) = \varphi_0 \delta(\tau) \tag{B-1}$$

where φ_0 is the amplitude, $\delta(\tau)$ is the Dirac Delta Function. τ is the difference of time of observations.

B.2 Random Constant

The random constant is a non-dynamic quantity with a fixed random amplitude. This can be defined by the differential equation:

$$\dot{x}(t) = 0 \tag{B-2}$$

The discrete form is defined by:

$$x_{k+1} = x_k \tag{B-3}$$

B.3 Random Walk

Random walk is produced when uncorrelated signals are integrated. The differential equation for this process is given by:

$$\dot{x}(t) = w(t) \tag{B-4}$$

where w is white Gaussian noise with a constant PSD. The discrete form is defined by:

$$x_{k+1} = x_k + w_k \tag{B-5}$$

B.4 First Order Gauss-Markov Process

A Gauss-Markov random process has exponential autocorrelation functions. The differential equation for this process is given by:

$$\dot{x}(t) = -\beta x(t) + \sqrt{2\sigma^2 \beta w(t)} \tag{B-6}$$

where $\sigma^2$is the variance of the process, β is the inverse of the process' time constant.

Appendix C Allan Variance Noise Terms

C.1 Quantization Noise

When an analog signal is converted into a digital signal, quantization noise is added to the signal. This noise is identified when a section of an AV log-log graph has a slope of -1. The relationship between the AV σ^2 and the quantization coefficient Q is:

$$\sigma^2(T) = \frac{3Q^2}{T^2} \quad \text{(C-1)}$$

The quantization coefficient Q can be found when $T = \sqrt{3}$. The units of Q are $\frac{m}{s}$ and $degrees$ for accelerometers and gyroscopes respectively.

C.2 Angle / Velocity Random Walk

This is a high frequency noise that affects a gyroscope with angular random walk and an accelerometer with velocity random walk, its correlation time is shorter than the sample time. This noise is identified when a section of an AV log-log graph has a slope of $-\frac{1}{2}$. The relationship between the AV σ^2 and the angle/velocity random walk coefficient Q is:

$$\sigma^2(T) = \frac{Q^2}{T} \quad \text{(C-2)}$$

The angle/velocity random walk coefficient Q can be found when $T = 1$. The units of Q are $m/s/\sqrt{h}$ and $degrees/\sqrt{h}$ for accelerometers and gyroscopes respectively.

C.3 Bias Instability

This noise is caused by the electronics of the sensor. This noise is identified when a section of an AV log-log graph has a slope of 0. A slope of 0 means that the AV standard deviation is uncorrelated with the cluster time, their relationship with the bias instability coefficient B is:

$$\sigma^2(T) = \frac{2ln2}{\pi} B^2 \quad \text{(C-3)}$$

Taking the square root of (2-10):

$$\sigma(T) = \sqrt{\frac{2ln2}{\pi}} B = 0.664B \quad \text{(C-4)}$$

The bias instability coefficient B can be found by dividing $\sigma(0)$ by 0.664. The units of B are $\frac{m}{s}/h$ and $degrees/h$ for accelerometers and gyroscopes respectively.

C.4 Rate Random Walk

The origin for this random process is unknown. This noise is identified when a section of an AV log-log graph has a slope of $+\frac{1}{2}$. The relationship between the AV σ^2 and the rate random walk coefficient K is:

$$\sigma^2(T) = \frac{K^2}{3}T \quad \text{(C-5)}$$

The rate random walk K can be found when $T = 3$. The units of K are $m/s/h^{\frac{3}{2}}$ and $degrees/h^{\frac{3}{2}}$ for accelerometers and gyroscopes respectively.

C.5 Rate Ramp

This is not a random error, rather deterministic, but it is very useful to check the behavior of $\sigma(T)$. This error is identified when a section of an AV log-log graph has a slope of $+1$. The relationship between the AV σ^2 and the rate random walk coefficient R is:

$$\sigma^2(T) = \frac{R^2T^2}{2} \quad \text{(C-6)}$$

The rate ramp error R can be found when $T = \sqrt{2}$. The units of K are $m/s/h^2$ and $degrees/h^2$ for accelerometers and gyroscopes respectively.

Appendix D Using the Levenberg-Marquardt Algorithm For Magnetometer Calibration

The ideal magnetic field intensity measured by a magnetometer is:

$$\|\boldsymbol{H}_d\| = \sqrt{H_{dx}^2 + H_{dy}^2 + H_{dz}^2} \tag{D-1}$$

Combining (D-1) with the magnetometer error model in (2-2), the total magnetic field intensity can be calculated by:

$$\|\boldsymbol{H}_d\|^2 = \boldsymbol{H}_d^T\boldsymbol{H}_d = (\boldsymbol{H}+\boldsymbol{\beta})^{\boldsymbol{T}}\,\boldsymbol{K}^{\boldsymbol{T}}\boldsymbol{K}\,(\boldsymbol{H}+\boldsymbol{\beta}) \tag{D-2}$$

From (2-16) a positive ellipsoid can be defined as:

$$\boldsymbol{H}^{\boldsymbol{T}}\frac{\boldsymbol{K}^{\boldsymbol{T}}\boldsymbol{K}}{\|\boldsymbol{H}_d\|^2}\boldsymbol{H} - \frac{2\boldsymbol{\beta}^{\boldsymbol{T}}\boldsymbol{K}^{\boldsymbol{T}}\boldsymbol{K}}{\|\boldsymbol{H}_d\|^2}\boldsymbol{H} + \frac{\boldsymbol{\beta}^{\boldsymbol{T}}\boldsymbol{K}^{\boldsymbol{T}}\boldsymbol{K}\boldsymbol{\beta}}{\|\boldsymbol{H}_d\|^2} = 1 \tag{D-3}$$

D.1 Sphere Fitting

The error model for a sphere of radius $\boldsymbol{R}$ is:

$$\boldsymbol{H} = \boldsymbol{H}_d - \boldsymbol{\beta} \tag{D-4}$$

$$R^2 = \|\boldsymbol{H}_d\|^2 = \boldsymbol{H}_d^T\boldsymbol{H}_d = (\boldsymbol{H}+\boldsymbol{\beta})^{\boldsymbol{T}}(\boldsymbol{H}+\boldsymbol{\beta}) \tag{D-5}$$

$$R^2 = \boldsymbol{H}^{\boldsymbol{T}}\boldsymbol{H} + 2\boldsymbol{H}^{\boldsymbol{T}}\boldsymbol{\beta} + \boldsymbol{\beta}^{\boldsymbol{T}}\boldsymbol{\beta} \tag{D-6}$$

Defining (2-20) as a radius function that depends on the measurements $\boldsymbol{H}$ and the center of the sphere $\boldsymbol{\beta}$:

$$f(\boldsymbol{H},\boldsymbol{\beta}) = \|\boldsymbol{H}^{\boldsymbol{T}}\boldsymbol{H} + 2\boldsymbol{H}^{\boldsymbol{T}}\boldsymbol{\beta} + \boldsymbol{\beta}^{\boldsymbol{T}}\boldsymbol{\beta}\|^{\frac{1}{2}} \tag{D-7}$$

We look to minimize the sum of squares of the deviations $S(R,\boldsymbol{\beta})$ of the perfect sphere with radius R, minus the sphere obtained from the measurements $f(\boldsymbol{H},\boldsymbol{\beta})$ to find the parameters $(R,\boldsymbol{\beta})$.

The L-M is an iterative process and requires an initial parameter. The initial parameters needed to fit a sphere to the data are the radius $\boldsymbol{R}_0$ and the sphere center coordinates $\boldsymbol{\beta}_0$.

$$(R,\boldsymbol{\beta})_{i+1} = (R,\boldsymbol{\beta})_i - [\boldsymbol{J}^{\boldsymbol{T}}\boldsymbol{J} + \boldsymbol{\lambda}\,diag(\boldsymbol{J}^{\boldsymbol{T}}\boldsymbol{J})]^{-1}\,\boldsymbol{J}^{\boldsymbol{T}}(R - f(\boldsymbol{H},\boldsymbol{\beta})) \tag{D-8}$$

$$\tau(i) = -[\boldsymbol{J}^{\boldsymbol{T}}\boldsymbol{J} + \boldsymbol{\lambda}\,diag(\boldsymbol{J}^{\boldsymbol{T}}\boldsymbol{J})]^{-1}\,\boldsymbol{J}^{\boldsymbol{T}}(R - f(\boldsymbol{H},\boldsymbol{\beta})) \tag{D-9}$$

where $\tau(i)$ is the direction of exploration and $\boldsymbol{\lambda}$ a damping parameter to control the direction of exploration and the step length in the iteration process. $\boldsymbol{J}$ Is the Jacobian matrix of the function $R - f(\boldsymbol{H}, \boldsymbol{\beta})$. The diagonal elements of $\boldsymbol{J^T J}$ are used to form the matrix $diag(\boldsymbol{J^T J})$

The term $R - f(\boldsymbol{H}, \boldsymbol{\beta})$ can be expressed as the function F:

$$F(\boldsymbol{H}, (R, \boldsymbol{\beta})) = R - f(\boldsymbol{H}, \boldsymbol{\beta}) \tag{D-10}$$

The Jacobian of function F is:

$$\boldsymbol{J}(i) = \frac{\partial F(\boldsymbol{H}(i), (R, \boldsymbol{\beta}))}{\partial (R, \boldsymbol{\beta})} \tag{D-11}$$

The error for measurement i is given by:

$$F(\boldsymbol{H}(i), (R, \boldsymbol{\beta})) = R - \left\| H_x^2 + H_y^2 + H_z^2 + 2H_x\beta_x + 2H_y\beta_y + 2H_z\beta_z + \beta_x^2 + \beta_y^2 + \beta_z^2 \right\|^{\frac{1}{2}} \tag{D-12}$$

To simplify:

$$a = \left\| H_x^2 + H_y^2 + H_z^2 + 2H_x\beta_x + 2H_y\beta_y + 2H_z\beta_z + \beta_x^2 + \beta_y^2 + \beta_z^2 \right\|^{\frac{1}{2}} \tag{D-13}$$

$$\frac{\partial F(\boldsymbol{H}, (R, \boldsymbol{\beta}))}{\partial R} = 1 \tag{D-14}$$

$$\frac{\partial F(\boldsymbol{H}, (R, \boldsymbol{\beta}))}{\partial \beta_x} = -(H_x - \beta_x)/a \tag{D-15}$$

$$\frac{\partial F(\boldsymbol{H}, (R, \boldsymbol{\beta}))}{\partial \beta_y} = -(H_y - \beta_y)/a \tag{D-16}$$

$$\frac{\partial F(\boldsymbol{H}, (R, \boldsymbol{\beta}))}{\partial \beta_z} = -(H_z - \beta_z)/a \tag{D-17}$$

The Jacobian matrix for measurement i is:

$$\boldsymbol{J}(i) = \left[1 \ -\frac{H_x - \beta_x}{a} \ -\frac{H_y - \beta_y}{a} \ -\frac{H_z - \beta_z}{a}\right] \tag{D-18}$$

The Jacobian for N measurements is:

$$\boldsymbol{J} = \left[N \ \sum_{i=1}^{N}\left(-\frac{H_x(i) - \beta_x}{a}\right) \ \sum_{i=1}^{n}\left(-\frac{H_y(i) - \beta_y}{a}\right) \ \sum_{i=1}^{N}\left(-\frac{H_z(i) - \beta_z}{a}\right)\right] \tag{D-19}$$

To start the iteration, initial values of $\boldsymbol{R}_0$, $\boldsymbol{\beta}_0$, and $\boldsymbol{J}$ are used as input to equation (2-22). The magnitude of the magnetic field for the first measurement can be used for $\boldsymbol{R}_0$ and to build $\boldsymbol{J}$. The initial center of the sphere $\boldsymbol{\beta}_0$ can be set to (0,0,0). The initial value of $\boldsymbol{\lambda}$ can be set to a large number.

To determine the direction of exploration, it is necessary to take the direction of decreasing values of the squared residual sum of all samples $S(R, \boldsymbol{\beta})$ which is computed after each iteration with:

$$S(R, \boldsymbol{\beta}) = \frac{\sum_{i=1}^{N}[R(i) - f(\boldsymbol{H}(\boldsymbol{i}), \boldsymbol{\beta}(\boldsymbol{i}))]^2}{N} \quad \text{(D-20)}$$

When the iteration has converged to or under a tolerance value, it will provide the estimated radius $\hat{R}$, which in turn is the magnitude of the magnetic field. It will also produce the estimated center of the sphere $\hat{\boldsymbol{\beta}}$ which corresponds to the "Hard Iron" error.

D.2 Ellipsoid Fitting

With the sphere being estimated, now the next step is to fit an ellipsoid to the measured data, and this is because the "Soft Iron" error deforms the sphere into a different shape which might be closer to an ellipsoid. The goal is to fit an ellipsoid that minimizes the sum of the squares of deviations $S(\hat{R}, \boldsymbol{\gamma})$, these deviations are the difference of the estimated sphere with radius $\hat{R}$ and the perfect fit ellipsoid $f(\boldsymbol{H}, \boldsymbol{\gamma})$ that is:

$$f(\boldsymbol{H}, \boldsymbol{\gamma}) = \|\boldsymbol{H}_d^T \boldsymbol{H}_d\|^{\frac{1}{2}} = \|\boldsymbol{H^T K^T K H} + \boldsymbol{2 H^T K^T K \beta} + \boldsymbol{\beta^T K^T K \beta}\|^{\frac{1}{2}} \quad \text{(D-21)}$$

where $\boldsymbol{K}$ is a symmetric matrix that corresponds to the "Soft Iron" error:

$$\boldsymbol{K} = \begin{bmatrix} k_{11} & k_{12} & k_{13} \\ k_{12} & k_{22} & k_{23} \\ k_{13} & k_{23} & k_{33} \end{bmatrix} \quad \text{(D-22)}$$

and $\boldsymbol{\gamma}$ is a nine-element vector that contains the "Hard Iron" error:

$$\boldsymbol{\gamma} = [k_{11} \quad k_{12} \quad k_{13} \quad k_{22} \quad k_{23} \quad k_{33} \quad \beta_x \quad \beta_y \quad \beta_z] \quad \text{(D-23)}$$

The Jacobian $\boldsymbol{J}$ for $f(\boldsymbol{H}, \boldsymbol{\gamma})$ is:

$$\boldsymbol{J} = \left[\sum_{i=1}^{N} J_1(i) \ \sum_{i=1}^{N} J_2(i) \ \sum_{i=1}^{N} J_3(i) \ \sum_{i=1}^{N} J_4(i) \ \sum_{i=1}^{N} J_5(i) \ \sum_{i=1}^{N} J_6(i) \ \sum_{i=1}^{N} J_7(i) \ \sum_{i=1}^{N} J_8(i) \ \sum_{i=1}^{N} J_9(i)\right] \quad \text{(D-24)}$$

where the elements of $\boldsymbol{J}$ are defined as:

$$J_1 = \frac{\partial f(\boldsymbol{H}, \boldsymbol{\gamma})}{\partial k_{11}} = -\frac{(H_x + \beta_x)A}{b} \quad \text{(D-25)}$$

$$J_2 = \frac{\partial f(\boldsymbol{H},\boldsymbol{\gamma})}{\partial k_{22}} = -\frac{(H_y+\beta_y)B}{b} \tag{D-26}$$

$$J_3 = \frac{\partial f(\boldsymbol{H},\boldsymbol{\gamma})}{\partial k_{33}} = -\frac{(H_z+\beta_z)C}{b} \tag{D-27}$$

$$J_4 = \frac{\partial f(\boldsymbol{H},\boldsymbol{\gamma})}{\partial k_{12}} = -\frac{(H_y+\beta_y)A+(H_x+\beta_x)B}{b} \tag{D-28}$$

$$J_5 = \frac{\partial f(\boldsymbol{H},\boldsymbol{\gamma})}{\partial k_{13}} = -\frac{(H_z+\beta_z)A+(H_x+\beta_x)C}{b} \tag{D-29}$$

$$J_6 = \frac{\partial f(\boldsymbol{H},\boldsymbol{\gamma})}{\partial k_{23}} = -\frac{(H_z+\beta_z)B+(H_y+\beta_y)C}{b} \tag{D-30}$$

$$J_7 = \frac{\partial f(\boldsymbol{H},\boldsymbol{\gamma})}{\partial \beta_x} = -\frac{k_{11}(H_x+\beta_x)+k_{12}(H_y+\beta_y)+k_{13}(H_z+\beta_z)}{b} \tag{D-31}$$

$$J_8 = \frac{\partial f(\boldsymbol{H},\boldsymbol{\gamma})}{\partial \beta_y} = -\frac{k_{12}(H_x+\beta_x)+k_{22}(H_y+\beta_y)+k_{23}(H_z+\beta_z)}{b} \tag{D-32}$$

$$J_9 = \frac{\partial f(\boldsymbol{H},\boldsymbol{\gamma})}{\partial \beta_z} = -\frac{k_{13}(H_x+\beta_x)+k_{23}(H_y+\beta_y)+k_{33}(H_z+\beta_z)}{b} \tag{D-33}$$

and the values of A, B, C and b are obtained by using:

$$A = k_{11}(H_x + \beta_x) + k_{12}(H_y + \beta_y) + k_{11}(H_z + \beta_z) \tag{D-34}$$

$$B = k_{12}(H_x + \beta_x) + k_{22}(H_y + \beta_y) + k_{23}(H_z + \beta_z) \tag{D-35}$$

$$C = k_{13}(H_x + \beta_x) + k_{23}(H_y + \beta_y) + k_{33}(H_z + \beta_z) \tag{D-36}$$

$$b = \|\boldsymbol{K}(\boldsymbol{H} + \boldsymbol{\beta})\| \tag{D-37}$$

The iterative formula for the L-M algorithm is now:

$$\boldsymbol{\gamma}_{i+1} = \boldsymbol{\gamma}_i - [\boldsymbol{J^T J} + \boldsymbol{\lambda}\, diag(\boldsymbol{J^T J})]^{-1}\, \boldsymbol{J^T}(\hat{R} - f(\boldsymbol{H},\boldsymbol{\gamma})) \tag{D-38}$$

The estimated values of $\hat{R}$, $\widehat{\boldsymbol{\beta}}$ and setting $\boldsymbol{K}$ as an identity matrix are used to get $\boldsymbol{\gamma}_0$ and the Jacobian $\boldsymbol{J}$, which is then the input to equation (2-52).

To determine the direction of exploration, it is necessary to take the direction of decreasing values of the squared residual sum of all samples $S(\boldsymbol{\gamma})$ which is computed after each iteration with:

$$S(\boldsymbol{\gamma}) = \frac{\sum_{i=1}^{N}[\hat{R} - f(\boldsymbol{H}(\boldsymbol{i}),\boldsymbol{\gamma}(\boldsymbol{i}))]^2}{N} \tag{D-39}$$

When the iteration has converged to or under a tolerance value, it will provide the estimated $\widehat{\boldsymbol{\gamma}}$, where the last three elements contain the "Hard Iron" error $\widehat{\boldsymbol{\beta}}$. The values estimated in $\boldsymbol{K}$ will contain the "Soft Iron" error.

Appendix E Extended Kalman Filter (EKF)

E.1 System Model

The system model has two models, the process and the measurement model given by:

$$\boldsymbol{x}_k = \boldsymbol{f}(x_{k-1},\ u_k,\ w_k) \tag{E-1}$$

$$\boldsymbol{z}_k = \boldsymbol{h}(x_k,\ v_k) \tag{E-2}$$

E.2 Important Assumptions

The system assumes a gaussian distribution with zero mean and a given covariance matrix:

$$\boldsymbol{w}_k \sim \boldsymbol{N}(0\,,\boldsymbol{Q}_k) \tag{E-3}$$

$$\boldsymbol{v}_k \sim \boldsymbol{N}(0\,,\boldsymbol{R}_k) \tag{E-4}$$

$$\boldsymbol{E}\left[w_k {w_j}^T\right] = \boldsymbol{Q}_k \delta_{k-j} \tag{E-5}$$

$$\boldsymbol{E}\left[v_k {v_j}^T\right] = \boldsymbol{R}_k \delta_{k-j} \tag{E-6}$$

$$\boldsymbol{E}\left[w_k {v_j}^T\right] = \boldsymbol{0} \tag{E-7}$$

E.3 Prediction

The prediction step is given by:

$$\hat{\boldsymbol{x}}^{-}{}_{k} = \boldsymbol{f}(\hat{x}^{+}{}_{k-1},\ u_k,\ 0) \tag{E-8}$$

$$\boldsymbol{P}_k^{-} = \nabla \boldsymbol{f}_{\boldsymbol{x}} \boldsymbol{P}^{+}{}_{k-1} \nabla {\boldsymbol{f}_{\boldsymbol{x}}}^{\boldsymbol{T}} + \nabla \boldsymbol{f}_{\boldsymbol{w}} \boldsymbol{Q}_k \nabla {\boldsymbol{f}_{\boldsymbol{w}}}^{\boldsymbol{T}} \tag{E-9}$$

E.4 Update

The update step is given by:

$$\boldsymbol{v}_k = \boldsymbol{z}_k - \boldsymbol{h}(\hat{\boldsymbol{x}}^{-}{}_{k-1},\ 0) \tag{E-10}$$

$$\boldsymbol{S}_{\boldsymbol{k}} = \nabla \boldsymbol{h}_{\boldsymbol{x}} \boldsymbol{P}^{-}{}_{k} \nabla {\boldsymbol{h}_{\boldsymbol{x}}}^{\boldsymbol{T}} + \nabla \boldsymbol{h}_{\boldsymbol{v}} \boldsymbol{R}_k \nabla {\boldsymbol{h}_{\boldsymbol{v}}}^{\boldsymbol{T}} \tag{E-11}$$

$$\boldsymbol{K}_{\boldsymbol{k}} = \boldsymbol{P}^{-}{}_{k} \nabla {\boldsymbol{h}_{\boldsymbol{x}}}^{\boldsymbol{T}} \boldsymbol{S}_{\boldsymbol{k}}^{-\boldsymbol{1}} \tag{E-12}$$

$$\hat{\boldsymbol{x}}^{+}{}_{k} = \hat{\boldsymbol{x}}^{-}{}_{k} + \boldsymbol{K}_{\boldsymbol{k}} \boldsymbol{v}_k \tag{E-13}$$

$$\boldsymbol{P}_k^{+} = (\boldsymbol{I} - \boldsymbol{K}_{\boldsymbol{k}} \nabla \boldsymbol{h}_{\boldsymbol{x}}) \boldsymbol{P}_k^{-} \tag{E-14}$$